



LJMU Research Online

Júlio, MP, Brinchmann, J, Zoutendijk, SL, Read, JI, Vaz, D, Kamann, S, Krajnović, D, Boogaard, LA, Steinmetz, M and Bouché, N

The MUSE-Faint survey. V. Constraining Scalar Field Dark Matter with Antlia B

<http://researchonline.ljmu.ac.uk/id/eprint/20557/>

Article

Citation (please note it is advisable to refer to the publisher's version if you intend to cite from this work)

Júlio, MP, Brinchmann, J, Zoutendijk, SL, Read, JI, Vaz, D, Kamann, S, Krajnović, D, Boogaard, LA, Steinmetz, M and Bouché, N The MUSE-Faint survey. V. Constraining Scalar Field Dark Matter with Antlia B. *Astronomy & Astrophysics*. ISSN 0004-6361 (Accepted)

LJMU has developed [LJMU Research Online](#) for users to access the research output of the University more effectively. Copyright © and Moral Rights for the papers on this site are retained by the individual authors and/or other copyright owners. Users may download and/or print one copy of any article(s) in LJMU Research Online to facilitate their private study or for non-commercial research. You may not engage in further distribution of the material or use it for any profit-making activities or any commercial gain.

The version presented here may differ from the published version or from the version of the record. Please see the repository URL above for details on accessing the published version and note that access may require a subscription.

For more information please contact researchonline@ljmu.ac.uk

<http://researchonline.ljmu.ac.uk/>

The MUSE-Faint survey

V. Constraining Scalar Field Dark Matter with Antlia B

Mariana P. Júlio^{1,2,3}, Jarle Brinchmann^{1,2,4}, Sebastiaan L. Zoutendijk⁴, Justin I. Read⁵, Daniel Vaz^{1,2}, Sebastian Kamann⁶, Davor Krajinović³, Leindert A. Boogaard⁷, Matthias Steinmetz³, and Nicolas Bouché⁸

¹ Instituto de Astrofísica e Ciências do Espaço, Universidade do Porto, CAUP, Rua das Estrelas, PT4150-762 Porto, Portugal

² Departamento de Física e Astronomia, Faculdade de Ciências, Universidade do Porto, Rua do Campo Alegre 687, PT4169-007 Porto, Portugal

³ Leibniz-Institut für Astrophysik Potsdam (AIP), An der Sternwarte 16, D-14482 Potsdam, Germany

⁴ Leiden Observatory, Leiden University, P.O. Box 9513, 2300 RA Leiden, The Netherlands

⁵ University of Surrey, Physics Department, Guildford, GU2 7XH, UK

⁶ Astrophysics Research Institute, Liverpool John Moores University, IC2 Liverpool Science Park, 146 Brownlow Hill, Liverpool L35RF, United Kingdom

⁷ Max Planck Institute for Astronomy, Königstuhl 17, 69117 Heidelberg, Germany

⁸ Univ. Lyon, Univ. Lyon1, ENS de Lyon, CNRS, Centre de Recherche Astrophysique de Lyon UMR5574, 69230, Saint-Genis-Laval, France

Received date / Accepted date

ABSTRACT

Aims. We use stellar line-of-sight velocities of Antlia B, a faint dwarf galaxy in the NGC 3109 association, to derive constraints on the fundamental properties of scalar field dark matter originally proposed to solve the small-scale problems faced by cold dark matter models.

Methods. We use the first spectroscopic observations of Antlia B, a distant ($d \sim 1.35$ Mpc) faint dwarf ($M_V = -9.7$, $M_\star \sim 8 \times 10^5 M_\odot$), from MUSE-Faint – a survey of ultra-faint dwarfs with the Multi Unit Spectroscopic Explorer. Through measurement of line-of-sight velocities for stars in the $1' \times 1'$ field-of-view, we identify 127 stars as members of Antlia B, allowing us to model its dark matter density profile with the Jeans modelling code GRAVSPHERE. We implement a model for scalar field dark matter into GRAVSPHERE and use this to place constraints on the self-coupling strength of this model.

Results. We find a virial mass of $M_{200} \approx 1.66_{-0.92}^{+2.51} \times 10^9 M_\odot$ and a concentration parameter of $c_{200} \approx 17.38_{-4.20}^{+6.06}$ for Antlia B. These results are consistent with the mass-concentration relations in the literature. We constrain the characteristic length scale of the repulsive self-interaction R_{TF} of the scalar field dark matter model to $R_{TF} \lesssim 180$ pc (68% confidence level), which translates to a self-coupling strength of $\frac{g}{m^2} \lesssim 5.2 \times 10^{-20} \text{ eV}^{-1} \text{ cm}^3$. The constraint on the characteristic length scale of the repulsive self-interaction is inconsistent with the value required to match the observations of cores of dwarf galaxies in the Local Group, suggesting that the cored density profiles of those galaxies are not caused by scalar field dark matter.

Key words. dark matter – galaxies: individual: Antlia B – stars: kinematics and dynamics – techniques: imaging spectroscopy

1. Introduction

Since dark matter was proposed as an additional component to explain the mass of galaxy clusters (Zwicky 1933) and the flat observed rotation curves of galaxies (Rubin et al. 1980, Bosma 1981), many more indications for the existence of dark matter have been found (see Bertone & Hooper 2018 for an extensive review of the history of dark matter). The presence of this non-baryonic matter is required to explain the behaviour of most structures existing in the Universe and the vast majority of the cosmological observations favour a cold dark matter plus dark energy scenario (Λ CDM model) - from sub-galactic and galactic scales (Dwarf Galaxies, e.g. Read et al. 2019), to clusters of galaxies (e.g. Massey et al. 2018), going up to the large scale structure (e.g. Springel et al. 2006, Baur et al. 2016), to cosmological scales (anisotropies of the Cosmic Microwave Background, Planck Collaboration et al. 2016), and is even able to explain the offsets between mass and light in weak lensing systems (e.g. Harvey et al. 2015) (see e.g. Ferreira 2021 for a review).

Λ CDM has been very successful at predicting and explaining the large-scale structure of the Universe and its evolution with time (e.g. Vogelsberger et al. 2014, Schaye et al. 2015), which has led to it now being considered the standard model of cosmology. However, when we look at smaller scales, with length scales smaller than ~ 1 Mpc and mass scales smaller than $\sim 10^{11} M_\odot$, pure dark matter structure formation simulations in the standard model starts to face numerous challenges (Bullock & Boylan-Kolchin 2017). Some of the well-known problems associated with small scales are the missing satellites problem (Klypin et al. 1999, Moore et al. 1999) - galaxies like the Milky Way should have significantly more bound dark matter subhaloes than the number of observed satellite galaxies; the too-big-to-fail (TBTf) problem (Boylan-Kolchin et al. 2011) - dwarf galaxies are expected to be hosted by haloes that are significantly more massive than indicated by the measured galactic velocity; and the core-cusp problem (Flores & Primack 1994, Moore 1994) - the observed cores of many dark-matter dominated galaxies are both less dense and less cuspy than predicted by the pure dark matter

N -body simulations in the standard model¹. One way to resolve these discrepancies could be to posit that we need a modified gravity model (see e.g. Clifton et al. 2012 for a review). While these offer an interesting pathway, they face several observational challenges on all scales (e.g. Clowe et al. 2006, Natarajan & Zhao 2008, Dodelson 2011, Ibata et al. 2011, Read et al. 2019). In this paper, we, therefore, choose to focus on ways to resolve these small-scale challenges within the Λ CDM model and its variants.

Three major scenarios have been proposed to solve the small-scale problems in Λ CDM. The first one implies that there might be problems with the data from the observations due to poor resolution (e.g. de Blok 2010) or due to misinterpretation of the data (e.g. Valenzuela et al. 2007, Oman et al. 2015). Another possibility is the lack of modelling of baryonic physics in the simulations. Adding baryons to the simulations can straightforwardly solve the missing satellite problem by an appropriate mapping of visible galaxies to dark subhaloes (e.g. Read & Erkal 2019). However, the cusp-core and TBTF problems are harder as they seem to imply that baryons need to physically move dark matter out of the centres of galaxies. Mechanisms have been proposed, however, in which repeated gas inflow-outflow and/or dynamical friction from dense clumps of gas or stars cause the gravitational potential to fluctuate with time. This allows energy to be transferred to dark matter particle orbits, pushing dark matter out of galaxy centres, making them more cored (e.g. Navarro et al. 1996, El-Zant et al. 2001, Nipoti & Binney 2014, Read et al. 2019). The last class of solutions, and perhaps the most exciting, conjectures that the nature of dark matter itself is different from the current paradigm. The proposed alternatives to the CDM cover a wide range of particle masses, from macroscopic objects (e.g. Massive Compact Halo Objects, Griest 1991; Primordial Black Holes, Hawking 1971) to axion-like particles (Preskill et al. 1983); as well as a wide range of different interactions between the dark matter particles, such as self-interaction through scattering (Carlson et al. 1992) or annihilation (Kaplinghat et al. 2000). Recently, DM models that involve ultra-light particles that have masses low enough to exhibit wave-like behaviour on astrophysical scales have been emerging. The free-field case of these models is called fuzzy dark matter (FDM; Dine & Fischler 1983, Preskill et al. 1983, Hu et al. 2000), with masses of the particles of 10^{-22} eV, can produce solitonic cores of size ~ 1 kpc, being able to reproduce the cores observed in the dwarfs of the Local Group (Hui et al. 2017). FDM is comprised of ultralight bosons that form a Bose-Einstein Condensate and is described by a complex scalar field. In this model, structure formation is inhibited below the de Broglie wavelength but behaves similarly to CDM on larger scales (Hu et al. 2000). Some models of ultra-light DM include interactions, that vary from single-field with self-interactions (Peebles 2000, Rindler-Daller & Shapiro 2012) to multi-field with non-trivial couplings (Matos et al. 2000, Bettoni et al. 2014, Berezhiani & Houry 2015). In this paper, we explore scalar field dark matter (SFDM; Lee & Koh 1996) as a modified model of Λ CDM. By modifying the microphysics of the dark matter, this model, just like FDM, diverges the most from CDM on small scales but behaves similarly to it on large scales, preserving the successful framework of the standard model (Li et al. 2014). However, in this case, the interactions between the particles give rise to a fluid

pressure that produces halo cores. Comparing the rotation curves of the haloes formed in this cosmology with the ones found in dwarf galaxies in the local Universe, SFDM-haloes are able to simultaneously address the ‘too-big-to-fail’ and the ‘cusp-core’ problems when a strong enough repulsive self-interaction is also present (Dawoodbhoy et al. 2021). A more detailed explanation of this model will be addressed later in this paper. In order to solve the small-scale problems, Dawoodbhoy et al. (2021) require a characteristic length scale of the model of $\gtrsim 1$ kpc. Li et al. (2014, 2017) constrain this value to $\lesssim 5$ kpc based on observations from the CMB temperature anisotropy power spectrum. These limits correspond to self-coupling strengths in the range $1.6 \times 10^{-18} \lesssim g/m^2 c^4 \lesssim 4 \times 10^{-17} \text{eV}^{-1} \text{cm}^3$ and require a particle mass larger than $\sim (2 - 10) \times 10^{-22} \text{eV}/c^2$. Shapiro et al. (2021), however, found, by using constraints on FDM as a proxy for SFDM, that the characteristic length scale of SFDM should be as low as 10 pc. Hartman et al. (2022) found this value to be < 1 kpc. These are, to our knowledge, the only constraints placed on the SFDM model described by Li et al. (2014).

To understand and solve small-scale challenges to the Λ CDM paradigm, we need to study the very smallest structures in the Universe. The most encouraging class of objects for this purpose are possibly ultra-faint dwarfs (UFDs). These galaxies are defined with an absolute magnitude of $M_V \gtrsim -8$ and have total luminosities below those of individual bright red supergiant stars. Their sizes are intermediate between typical globular clusters (GCs) and low-luminosity dwarf spheroidal galaxies (Willman & Strader 2012). UFDs represent the extreme limit of the galaxy formation process: they have the lowest metallicities, oldest ages, smallest sizes, and smallest stellar masses of all known galaxies (Simon 2019). Unlike most of the larger systems, they have survived to the present day as relics from the early universe. These objects, therefore, present us with a unique window into the conditions prevalent at the time when the first galaxies were forming (see e.g. Bovill & Ricotti 2011, Wheeler et al. 2015). Furthermore, they reside in the smallest dark matter haloes yet found and have almost negligible baryonic mass, which means that their dynamical mass-to-light ratios are the highest ever measured (Simon 2019). Additionally, baryonic feedback should not significantly influence the dark matter density profiles of UFDs (Orkney et al. 2021), since they do not have enough stars to have significant supernovae feedback (Peñarrubia et al. 2012). Because of all these arguments, UFDs have attracted a lot of attention in the last few years. The known number of these objects has been increasing over the past several years due to photometric catalogues from imaging surveys, and most of them are MW satellites. Thus, the density profiles and the measured central densities of UFDs can help us to constrain the nature of dark matter and its properties, making these objects unprecedented laboratories for understanding the behaviour of dark matter on small scales (see e.g. Calabrese & Spergel 2016, Errani et al. 2018, Bozek et al. 2018).

However, the faintness of UFDs makes it challenging to obtain large numbers of stellar line-of-sight velocities and thus high-precision density profiles. Antlia B (Ant B), a slightly brighter dwarf galaxy ($M_V = -9.7$, $M_\star \sim 8 \times 10^5 M_\odot$), promises more data, while at this stellar mass, it is still expected that any star formation induced core would be very small (e.g. Bullock & Boylan-Kolchin 2017, Orkney et al. 2021). This makes Antlia B well suited for testing models of dark matter and we here present an in-depth analysis of the kinematics of Ant B (Zoutendijk et al. 2021b) from MUSE-Faint (Zoutendijk et al. 2020), a survey of UFDs with the Multi Unit Spectroscopic Explorer (MUSE) (Bacon et al. 2010). With these data, which cover a wide range of

¹ Note that the TBTF problem can also be understood as the cusp-core problem but for satellites. That is to say, the TBTF can be solved if (some) satellite dwarf galaxies have dark matter cores similar to those found in isolated dwarfs (see e.g. Read et al. 2006, Read & Erkal 2019).

radii, and adopting the Jeans analysis code `GRAVSPHERE` (Read & Steger 2017), we are able to derive the dark matter density profile of Ant B and, ultimately, to place constraints on the properties of scalar field dark matter.

In Sect. 2 we describe the observations (Sect. 2.1), summarise the data reduction (Sect. 2.2) and describe the selection of the members of our dwarf, showing the determination of line-of-sight velocities from the spectra as well as its velocity distribution. (Sect. 2.3). This is followed in Sect. 3 by the models of dark matter used in this paper (Sect. 3.1), by a brief description of the analysis tool used, `GRAVSPHERE` (Sect. 3.2), and by the priors used for each model (Sect. 3.3). We continue in Sect. 4 with our results on the constraints of the properties of the studied dark matter models (Sect. 4.1), and the recovered dark matter density profiles (Sect. 4.2). We end with a discussion in Sect. 5 and our conclusions in Sect. 6. In Appendix A we show the numerical implementation of the SFDM model, presented in Sect. 3.1. The fitted parameters by `GRAVSPHERE` are presented in Appendix B, followed by the relevant plots to discuss the robustness of the dark matter constraints obtained in Appendix C.

2. Antlia B

Antlia B was discovered by Sand et al. (2015) as a companion to NGC 3109 using DECam at Cerro Tololo International Observatory. Deep optical *Hubble Space Telescope* (*HST*) images that followed the ground-based discovery of this dwarf were presented by Hargis et al. (2020). The photometric data obtained in both of these studies allowed for the measurement of structural properties that were adopted in the present paper, listed in Table 1.

Table 1. Properties of Antlia B.

Parameter	Value	Source
RA (deg)	147.2337	Sand et al. (2015)
Dec. (deg)	-25.9900	Sand et al. (2015)
D (Mpc)	1.35 ± 0.06	Hargis et al. (2020)
M_V (mag)	-9.7 ± 0.6	Sand et al. (2015)
r_h (pc)	273 ± 29	Sand et al. (2015)

Notes. (RA, Dec): coordinates of the centre of the galaxy; D : distance; M_V : absolute magnitude in the V -band; r_h : half-light radius.

Both studies agree that this dwarf has two distinct stellar populations: an old and metal-poor red giant branch population (>10 Gyr, $[\text{Fe}/\text{H}] \sim -2$), and a younger and more metal-rich population ($\approx 200 - 400$ Myr, $[\text{Fe}/\text{H}] \approx -1$). The theoretical isochrones for both of these populations were shown by Sand et al. (2015) and Hargis et al. (2020), and there is no evidence of recent star formation (≤ 10 Myr). The star formation history measured by Hargis et al. (2020) is compatible with the star formation seen in dwarf irregular galaxies in the Local Group: there is a constant growth in mass for the first ≈ 10 Gyr and a rise in the star formation in the last $\approx 2 - 3$ Gyr.

Sand et al. (2015) obtained $H\alpha$ imaging of Ant B and showed that the non-detection implied the lack of a stellar population with age <100 Myr.

These studies focused on photometry and did not have spectroscopic data, thus the dynamical properties of the stellar popu-

lation have not been characterised. This is rectified by the present work.

2.1. Observations

Ant B was observed with MUSE (Bacon et al. 2010) on Unit Telescope 4 of the Very Large Telescope (VLT). MUSE is an optical wide-field spectrograph that uses the image slicing technique to cover a field of view of $1' \times 1'$ in wide-field mode with a spatial sampling of $0.2'' \times 0.2''$ (Bacon et al. 2017). The moderate spectral resolution (FWHM = $[2.4, 3] \text{ \AA}$), broad wavelength range ($[4650, 9300] \text{ \AA}$), good stability and relatively large field of view, allow the efficient acquisition of spectra of very faint stars, making MUSE an ideal instrument to study compact UFDs (Zoutendijk et al. 2020).

The 18 exposures total 4.5h, each one with an exposure time of 15 minutes, and were taken during the Guaranteed Time Observing (GTO, ESO ID 100.D-0807) runs between 11 and 15 February 2018 (9 exposures), between 14 and 18 March 2018 (6 exposures), and between 11 and 18 April 2018 (3 exposures). Observations followed a standard pattern of small dithers plus 90-degree rotation between each exposure.

2.2. Data reduction

The data reduction procedure used in this work follows the one described in Zoutendijk et al. (2021a). In brief, we adopted the standard method for reducing MUSE data with the MUSE Data Reduction Software (Weilbacher et al. 2020), complemented with a bad-pixel table from Bacon et al. (2017). Next, the produced data cube was post-processed with the Zurich Atmosphere Purge (version 2.0; Soto et al. 2016) to remove residual sky signatures.

We used the public images of Ant B from the *HST* (HST-GO-14078; PI: J. Hargis) in the V-band (F606W filter) and another in the I-band (F814W filter) in order to create a photometric catalogue using `SExtractor` (Bertin & Arnouts 1996).

Spectra

We extracted spectra of the stellar sources in the MUSE cube using the `PAMPELMUSE` code (Kamann et al. 2013). Positions and magnitudes for the stellar sources, used as input to `PampelMuse`, were extracted from the *HST* catalogue previously created with `SExtractor`. In summary, `PAMPELMUSE` determines an initial point-spread function (PSF) in the MUSE data, which is modelled with an analytic Moffat profile. After identifying in the reference catalogue the sources for which it is feasible to extract spectra, the spectra are extracted by simultaneously fitting a PSF to all sources that have been identified as resolvable. Since our field of view is very crowded, it was necessary to change the default value of `apernois`, the parameter that defines the maximum fraction of contaminating flux by nearby sources inside a PSF aperture. This parameter was changed from 0.1 to 0.4, meaning that the maximum allowed contamination around a PSF source from a neighbouring source has to be smaller than this value. In total, 2514 spectra were extracted with `PAMPELMUSE`.

Line-of-sight velocities

The line-of-sight velocities were determined from the spectra collected from `PAMPELMUSE` using `SPEXXY` (Husser 2012). This

software allows the determination of stellar properties by comparing spectra with synthetic spectra.

We adopted the same grid of synthetic PHOENIX spectra (the Göttingen Spectral Library; Husser et al. 2013) used by Husser et al. (2016) for the globular cluster NGC 6397, by Roth et al. (2018) for the nearby galaxy NGC 300 and Zoutendijk et al. (2020) for the ultra-faint dwarf Eridanus II. The models are calculated on a grid of effective temperature T_{eff} , logarithm of surface gravity $\log g$, iron abundance $[\text{Fe}/\text{H}]$, and alpha-element abundance $[\alpha/\text{Fe}]$, and for each model the line broadening σ and line-of-sight velocity v_{LOS} can be fit. We fixed $[\alpha/\text{Fe}]$ to zero (solar) since the quality of the spectra is not high enough to differentiate between different values of this parameter. The free parameters are determined by a weighted non-linear least squares minimisation against high-resolution synthetic spectra. The uncertainties determined by SPEXXY underestimate the scatter in the velocities below a signal-to-noise ratio (SNR) of 5 (Kamann et al. 2016) so we only retain spectra with a SNR above or equal to this for the subsequent analysis. Out of the 2514 extracted spectra with PAMPELMUSE, 141 satisfied this criterion.

SPEXXY was able to determine a velocity and metallicity, as well as their associated uncertainties, for 131 of the 141 spectra with $\text{SNR} > 5$. For the other 10 spectra, the fit failed to converge, and they were left out.

To obtain photometry for the stars, we cross-matched our catalogue with the Hargis et al. (2020) catalogue - all of our sources had counterparts in this catalogue.

2.3. Selecting member stars

We discuss our member selection in greater detail in the companion paper Brinchmann et al. (in prep) but we summarise it here briefly.

To clean up our list of possible members, we compared the *HST* photometry against PARSEC (Bressan et al. 2012) isochrones. We adopted the metallicities and ages estimated by Hargis et al. (2020) and found that all 131 member stars were consistent with at least one isochrone at the distance of Antlia B. We also inspected all spectra manually to verify that they were all stellar spectra.

For the analysis here we also needed to exclude strong outliers in velocity. To do this we calculate the mean ($\mu \approx 370.5 \text{ km s}^{-1}$) and standard deviation of the velocities of the 131 candidate stars ($\sigma \approx 42.4 \text{ km s}^{-1}$) and excluded stars outside $\mu \pm 2\sigma$ (see Figure 1). This excluded four clear outliers in velocity, leading to a final sample of 127 member stars.

As discovered by Sand et al. (2015), Ant B has H I gas at a velocity of $v_{\text{H I}} = 376 \pm 2 \text{ km s}^{-1}$. The good agreement in line-of-sight velocity is encouraging and confirms that the stars and H I are associated. We then continued our analysis with 127 member stars of Ant B. These members are represented in Figure 2. The velocities of these members have been previously presented by Zoutendijk et al. (2021b) and the resulting catalogue can be found there.

Velocity distribution

In order to determine the intrinsic mean value and dispersion of the velocity of Ant B, it is necessary to take into account the associated measurement uncertainties. To this purpose, we adopt a Markov Chain Monte Carlo (MCMC) approach (see e.g. Hargreaves et al. 1994, Martin et al. 2018) described in detail in Zoutendijk et al. (2020), which assumes that the velocity distribution

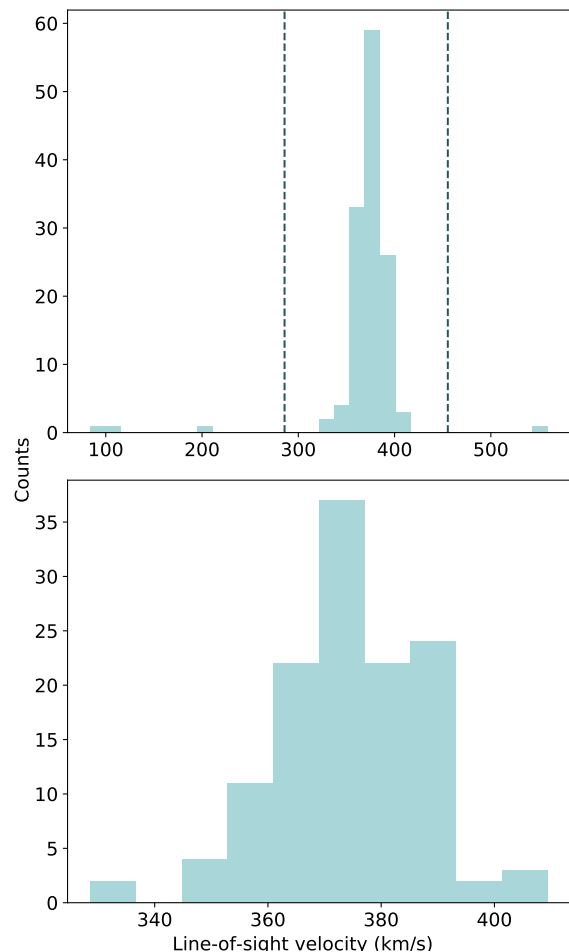


Fig. 1. **Top:** Histogram of the velocity for Antlia B candidates (131 stars) with the velocity cut $v = \mu \pm 2\sigma$ represented by the dashed lines. **Bottom:** Histogram of the velocity for Antlia B candidates (127 stars) after the velocity cut.

of the stars can be modelled with a Gaussian. The global likelihood of the system is then

$$\mathcal{L}(\mu, \sigma | v_i, \sigma_i) = \prod_i \left[\frac{1}{\sqrt{2\pi}\sigma_{\text{obs},i}} \exp\left(-\frac{1}{2} \left(\frac{v_i - \mu}{\sigma_{\text{obs},i}}\right)^2\right) \right], \quad (1)$$

where v_i is the velocity of star i , μ is the mean line-of-sight velocity of the system and $\sigma_{\text{obs},i}^2 = \sigma^2 + \sigma_i^2$ is the observed velocity dispersion for star i . We adopt a flat prior on μ between $[285.7, 455.3] \text{ km s}^{-1}$ to be consistent with our member selection. We also adopt a flat prior on σ between 0 and 40 km s^{-1} . The results are robust to the choice of prior.

We obtained a mean value of $v_{\text{LOS}} = 375.39^{+0.98}_{-0.97} \text{ km s}^{-1}$ and an intrinsic velocity dispersion of $\sigma_{v_{\text{LOS}}} = 7.87^{+1.02}_{-0.98} \text{ km s}^{-1}$. The resulting corner plot is represented in Figure 3. We see that there is good agreement between the mean velocity of the stars and the mean velocity of the H I gas reported by Sand et al. (2015).

3. Methods

We start by describing the dark-matter models tested in this paper in section 3.1. This is followed in 3.2 by the presentation of the analysis tool (GRAVSPHERE; Read & Steger 2017, Read et al. 2018, Genina et al. 2020, Read et al. 2019, Collins et al. 2021)

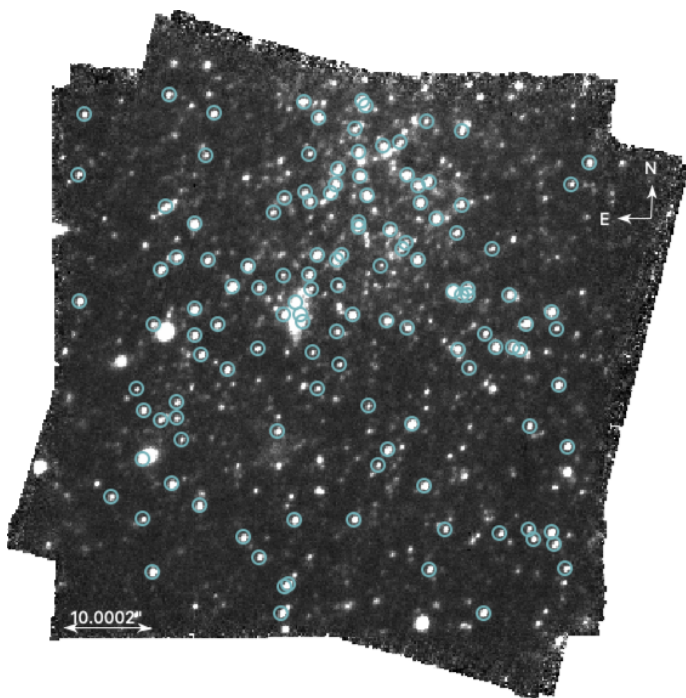


Fig. 2. Image of the final cube (all the exposures described before were combined in the data reduction) with the 127 stars identified as Ant B members represented by the blue circles.

used to constrain the dark matter profiles and their microphysical properties.

3.1. Models of dark matter density profiles

Cold dark matter

We adopt the Navarro-Frenk-White (NFW, Navarro et al. 1996) profile as the parametric description of cold dark matter density profiles,

$$\rho_{\text{CDM}}(r) = \frac{\rho_0}{(r/r_s)(1+r/r_s)^2}, \quad (2)$$

where the characteristic density, ρ_0 , is defined by $\rho_0 = \rho_{\text{crit}} \Delta^3 c_{200} g_c / 3$, and the scale radius, r_s , by $r_s = r_{200} / c_{200}$. ρ_{crit} is the critical density defined by $\rho_{\text{crit}} = 3H^2 / 8\pi G$, where H is the Hubble constant and G the gravitational constant. Finally, the virial radius r_{200} is defined by

$$r_{200} = \left[\frac{3}{4} M_{200} \frac{1}{\pi 200 \rho_{\text{crit}}} \right]^{1/3}, \quad (3)$$

where M_{200} is the virial mass enclosed in the virial radius. $\Delta \sim 200$ is an overdensity constant relative to the background matter density, c_{200} a concentration parameter, and g_c is defined as

$$g_c = \frac{1}{\log(1 + c_{200}) - \frac{c_{200}}{1 + c_{200}}}. \quad (4)$$

Scalar field dark matter

Scalar field dark matter (Li et al. 2014) is comprised of ultralight bosons and is described by the coupled Schrödinger-Poisson equations. This model is an alternative to Λ CDM and in this

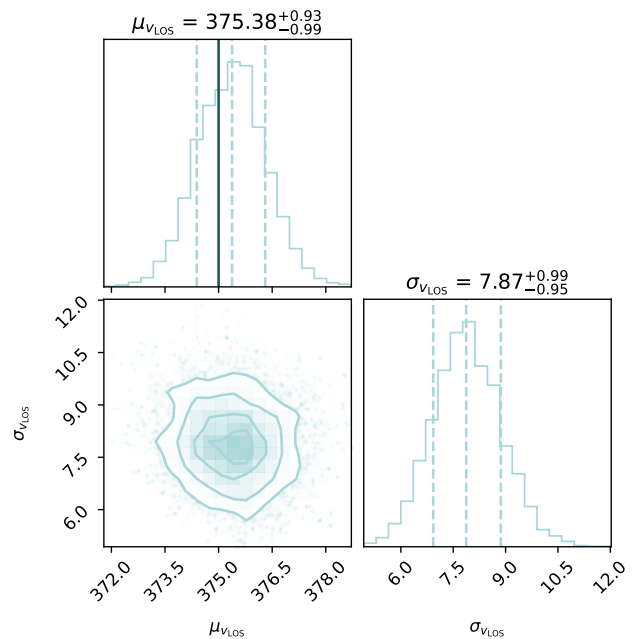


Fig. 3. Corner plot for the MCMC velocity fit, using the 127 member stars of Ant B. The histograms along the diagonal represent the posterior distribution for each parameter: the mean value μ_V in the top panel and the dispersion σ_V in the bottom right. The vertical dashed lines indicate the median and 68% confidence interval. The bottom left panel represents the 2D posterior distributions of both of these parameters, with the contours corresponding to 0.5σ , 1σ , 1.5σ and 2σ confidence levels, where σ is the standard deviation of the 2D distribution. The solid dark blue line in the top panel indicates the mean velocity of the H I gas reported by Sand et al. (2015).

case, it leads to a Bose-Einstein condensate and quantum superfluid. Just like fuzzy dark matter, this model's behaviour approaches the CDM model on large scales and differs the most on small scales. The main difference between SFDM and FDM is that SFDM also includes a repulsive self-interaction (Dawoodbhoy et al. 2021).

While CDM is described by the collisionless Boltzmann equation, SFDM obeys the nonlinear Schrödinger equation (NLSE) rewritten in terms of quantum hydrodynamics equations for the conservation of mass and momentum.

In the SFDM model, there are two length scales that characterise the scale below which the structure is suppressed. On the one hand we have the de Broglie wavelength $\lambda_{\text{deB}} = h/mv$, which is characteristic of the FDM model (in the case where self-interaction (SI) is not present - the free field limit) and depends on the boson mass m and its characteristic velocity v . On the other hand, we have λ_{SI} , resulting from the presence of a repulsive SI.

In FDM, structure formation is suppressed on scales below λ_{deB} . In the presence of the repulsive SI with self-coupling strength g , $\lambda_{\text{SI}} \propto \sqrt{g/m^2}$, and if the interaction is strong enough that $\lambda_{\text{SI}} \gg \lambda_{\text{deB}}$, structure is suppressed below λ_{SI} . In this regime, the Thomas-Fermi (TF) regime, λ_{deB} is much smaller than the characteristic length scale of the repulsive self-interaction, R_{TF} , given by

$$R_{\text{TF}} = \pi \sqrt{\frac{g}{4\pi G m^2}}. \quad (5)$$

This quantity is a physical constant of SFDM since it is fixed by the particle parameters (m, g) in their combination g/m^2 , called the SI strength parameter. R_{TF} is the relevant scale below which the Thomas-Fermi regime of SFDM differs from CDM. To avoid the small-scale structure problems for the standard model discussed before, either λ_{deb} for the FDM model, or λ_{SI} for the SFDM-TF model, should be ~ 1 kpc.

The density profile of the haloes formed in SFDM-TF was fitted by Dawoodbhoy et al. (2021) and is given by

$$\rho_{\text{SFDM}} = \begin{cases} \rho_c \text{sinc}(\pi r/R_{\text{TF}}) & r \leq \alpha R_{\text{TF}} \\ \rho_{\text{CDM}} & r \geq \alpha R_{\text{TF}} \end{cases}, \quad (6)$$

where $\text{sinc}(x) = \sin(x)/x$, ρ_c is the central density and α is a given fraction of R_{TF} determined by requiring mass conservation and density continuity at $r = \alpha R_{\text{TF}}$. As is clear from this equation, SFDM-TF behaves just like the CDM model on scales larger than R_{TF} .

3.2. GRAVSPHERE

To measure the dark-matter density profiles of Ant B, we use the updated version of GRAVSPHERE Jeans modelling code². A detailed explanation of its implementation can be found in Read & Steger (2017) and Read et al. (2018) which we briefly mention here for the reader's convenience.

GRAVSPHERE solves the Jeans equation (Jeans 1922) for our member stars while assuming that the stellar system is spherical, non-rotating, and in a steady state given by

$$\frac{1}{v_\star} \frac{\partial}{\partial r} (v_\star \sigma_r^2) + \frac{2\beta(r)\sigma_r^2}{r} = -\frac{GM(< r)}{r^2}, \quad (7)$$

where

$$\sigma_r^2 = \langle v_r^2 \rangle - \langle v_r \rangle^2 \text{ with } \langle v_r^n \rangle = \int v_r^n f d^3\mathbf{v}, \quad (8)$$

and $M(< r)$ is the total cumulative mass as a function of radius r . The tracer number density v_\star characterises the radial density profile of a population of massless tracers (in our case, stars moving in a galaxy) that move in the gravitational potential of its mass distribution $M(r)$, modelled with three Plummer (1911) profiles

$$v_\star(r) = \sum_{j=1}^3 \frac{3M_j}{4\pi a_j^3} \left(1 + \frac{r^2}{a_j^2}\right)^{5/3}, \quad (9)$$

with masses M_j and scale length a_j for each individual component. This allows us to recover the density profile $\rho(r)$ and the velocity anisotropy profile $\beta(r)$ of the studied stellar systems (Read & Steger 2017). The velocity anisotropy $\beta(r)$ is defined as

$$\beta(r) = \beta_0 + \frac{\beta_\infty - \beta_0}{1 + (r_0/r)^\eta}, \quad (10)$$

where β_0 is the central value of the anisotropy, β_∞ is the value at infinity, r_0 is a transition radius and η is the steepness of the transition. To avoid infinities, a symmetrised version of $\beta(r)$ is used

$$\tilde{\beta}(r) = \frac{\sigma_r(r) - \sigma_t(r)}{\sigma_r(r) + \sigma_t(r)} = \frac{\beta(r)}{2 - \beta(r)}. \quad (11)$$

² The newest version of this code is available for download at <https://github.com/justinread/gravsphere> (Collins et al. 2021).

$\tilde{\beta} = 0$ corresponds to an isotropic velocity dispersion; $\tilde{\beta} = 1$ corresponds to a fully radial dispersion; and $\tilde{\beta} = -1$ to a fully tangential distribution.

GRAVSPHERE relies on higher order moments of the velocity distribution via the fourth order Virial Shape Parameters (VSPs) (Merrifield & Kent 1990) to partially break the degeneracy that exists between the radial velocity dispersion (and therefore the cumulative mass distribution) and the velocity anisotropy. To bin the data in bins of projected radius R , we use an algorithm called BINULATOR (Collins et al. 2021).

After performing the BINULATOR routine, we apply our adaptation of GRAVSPHERE³ to Ant B data in order to get our dark matter density profile and, consequently, the dark matter constraints we are looking for. GRAVSPHERE solves the Jeans equation for the projected velocity dispersion. It also fits the two VSPs, with the initial guesses being the profiles estimated by BINULATOR.

GRAVSPHERE uses the ensemble sampler EMCEE (Foreman-Mackey et al. 2013) to fit the model to the data. Each individual Markov chain (walker) communicates with the other walkers at each step, contrary to the classic Metropolis-Hastings algorithm. Hence, it allows the chains to sample the posterior distribution more efficiently (Genina et al. 2020). The number of walkers and steps used depends on the model considered since some models require more time to achieve convergence. The first half of the steps generated are always discarded as a conservative burn-in criterion.

3.3. Priors

The standard priors that GRAVSPHERE requires were kept to their default values that we summarise here for convenience. We use priors on the symmetrised velocity anisotropy of: $-1 < \tilde{\beta}_0 < 1$; $-1 < \tilde{\beta}_\infty < 1$; $-1 < \log_{10}(r_0/\text{kpc}) < 0$; and $1 < \eta < 3$. We use a flat prior on the stellar mass of $6 < M_\star/(10^5 M_\odot) < 10$.

For the CDM model, the only quantities that we need to know in order to calculate all the other parameters are M_{200} and c_{200} , since $r_s = r_{200}/c_{200}$ and r_{200} can be estimated by Equation 3 (depends only on M_{200} and some constants), and g_c by Equation 4 (only depends on c_{200}).

Although we do not know the exact values of these parameters for the systems that we aim to study, the smallest dwarf galaxies show $M_{200} \approx 10^8 M_\odot$ (Bullock & Boylan-Kolchin 2017). Such a limit is also theoretically expected, since below this mass, galaxy formation becomes extremely inefficient due to hindered atomic cooling (e.g. Finkelstein et al. 2019). To be considered small-scale, the maximum value that M_{200} can take is approximately $10^{11} M_\odot$ (Bullock & Boylan-Kolchin 2017). For this reason, we use a generous flat prior on M_{200} ranging from $M_{200} = 10^{7.5} M_\odot$ to $M_{200} = 10^{11.5} M_\odot$, that encompasses the mass-range of all dwarf galaxies (Collins & Read 2022).

The concentration parameter c_{200} is related to M_{200} . We use the mass-concentration relation for cold dark matter derived by Gilman et al. (2019), based on observations of strong lenses, to determine a prior for the concentration parameter that is proper for a galaxy with the mass of Ant B. Since the covered mass range of this relation ($M_{200} = [10^6, 10^{10}] M_\odot$) is very similar to what we use, it seems appropriate to use the resulting values of the concentration parameter. They constrained the concentration at $z = 0$ with a 95% confidence of $c = 15_{-11}^{+18}$ for $M_{200} = 10^7 M_\odot$ and $c = 10_{-7}^{+14}$ for $M_{200} = 10^9 M_\odot$. Since we explore not only

³ The alternative dark matter models implemented are available for download at https://github.com/marianajulio/alternative_models_for_gravsphere.

CDM but also SFDM, we assume a generous flat prior for the concentration parameter is then $c = [1, 50]$. These values are described in the two top rows of Table 2.

Since this model has a straightforward density and mass profile, it does not need a high number of walkers and steps to converge. It was found that using $n_{\text{walkers}} = 250$ and $n_{\text{steps}} = 25000$ was sufficient to achieve convergence, making it the fastest model to run. Several runs were made with different values for these parameters and the final results were not affected by this choice.

The parameters of the SFDM density profile that require priors are M_{200} , c_{200} , and R_{TF} . For M_{200} and c_{200} we adopt the same priors as for the CDM profile, but we note that it has not been established that the mass-concentration relation established for CDM applies to SFDM. For that reason, we keep the priors quite broad. R_{TF} is chosen to take into account the possible values of this parameter discussed by Dawoodbhoy et al. (2021). This parameter is zero when a core is not present and the density profile follows the CDM model and needs to be ≥ 1 kpc in order to solve the core-cusp problem and the too-big-to-fail problem for Local Group dwarfs. However, $R_{\text{TF}} \leq 5$ kpc is required based on observations from the CMB temperature anisotropy power spectrum if we consider dark matter as SFDM (Dawoodbhoy et al. 2021), so our flat prior on R_{TF} varies from 0.001 kpc to 5 kpc.

Table 2. Priors used for the discussed dark matter models. CDM only uses the top two rows, while SFDM uses all priors.

Parameter	Min.	Max.
$\log_{10}(M_{200}/M_{\odot})$	7.5	11.5
c_{200}	1	50
R_{TF} (kpc)	0.001	5

Contrary to the CDM model, the SFDM model has to obey certain conditions to arrive at a physical solution for the density and mass profile. The implemented numerical parametrization of this model is discussed in detail in Appendix A. Although α and ρ_c are easily computed, all r must be evaluated in order to choose which calculation to perform next: either the density and mass profile associated with the TF regime, or the ones associated with the CDM model. Furthermore, to calculate the mass profile associated with the TF regime, an integral must be solved. Moreover, this model needs a higher number of walkers and steps to converge than did the CDM model - we used $n_{\text{walkers}} = 500$ and $n_{\text{steps}} = 10^5$ to get robust results.

4. Results

Using GRAVSPHERE, discussed in Sect. 3.2, we sample the parameter spaces of our implemented dark-matter density models, examined in Sect. 3.1. To do this, we use the kinematical measurements of Ant B, discussed in Section 2. Here, in Sect. 4.1, we present the obtained dark matter constraints and, in Sect. 4.2, the recovered density profiles as well as their comparison.

To achieve this goal, we need the kinematic and photometric data of Ant B. BINULATOR starts by fitting the photometric data in order to get the light profile. In our case, we made a mock photometric catalogue by drawing 10.000 sample photometric positions from the exponential distribution from Sand et al. (2015) and used them as photometric observations in BINULATOR. Next,

the 127 member stars of Ant B were binned radially from the centre of Ant B (listed in Table 1) into 5 bins, each of them having ~ 25 sources. The binned data that GRAVSPHERE uses is described in Table 3. Figure 4 shows the projected radii for all the stars, their position after the binning routine, and the velocity dispersion associated with each one of the bins in dark blue.

Table 3. Kinematic data of Ant B after the binning routine performed by BINULATOR, as used by GRAVSPHERE. The bins are represented by the mean projected radius of the stars in each bin.

Radius (kpc)	Velocity dispersion (km s ⁻¹)
0.031	$2.20^{+1.71}_{-1.06}$
0.089	$6.98^{+1.66}_{-2.30}$
0.140	$11.41^{+2.10}_{-2.23}$
0.198	$8.18^{+2.05}_{-2.32}$
0.283	$10.46^{+1.87}_{-2.09}$

Our best-fitting CDM and SFDM models are shown in Figure 4, compared with the stellar velocity dispersion data. Both models fit reasonably well the data but do not reproduce all features. Particularly, both models have difficulties in fitting the low central velocity dispersion when they are anchored at the half-light radii. This figure also shows that, as expected, we lack constraining power where there is no data - both at small (~ 10 pc) and large radii (≥ 1 kpc). The recovered fits from GRAVSPHERE for the VSPs and surface brightness profile can be seen in Figure B.2 of the Appendix.

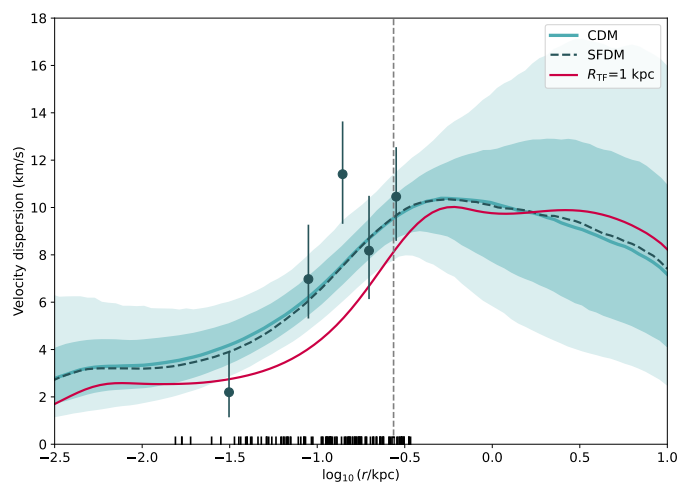


Fig. 4. Velocity dispersion of Ant B. The dark blue points represent the binned velocity dispersion with their associated uncertainties. The best fit from GRAVSPHERE for the CDM model is shown as a solid light blue line, with the light blue shaded regions showing the 68% and 95% confidence intervals for the CDM model. The dashed dark blue line represents the best fit for the SFDM model. Since the best fit for both models is so similar, the confidence intervals for the SFDM model are omitted for clarity. The half-light radius is represented by the vertical dashed line and the bottom marks represent the projected radii of the members of Ant B. The solid red line represents the shape that the velocity dispersion would have if $R_{\text{TF}} = 1$ kpc, keeping the other parameters with the same values as the best fit for the SFDM profile.

4.1. Dark matter constraints

The constraints of the physical parameters of the CDM and SFDM models are displayed in Figures 5 and 6, respectively. The constraints in the computational parametrizations for the SFDM are shown in Figure A.1 of the Appendix. To calculate the marginalised constraints, we took the median and quartiles of the chains after discarding samples with a χ^2 larger than 10 times the minimum χ^2 .

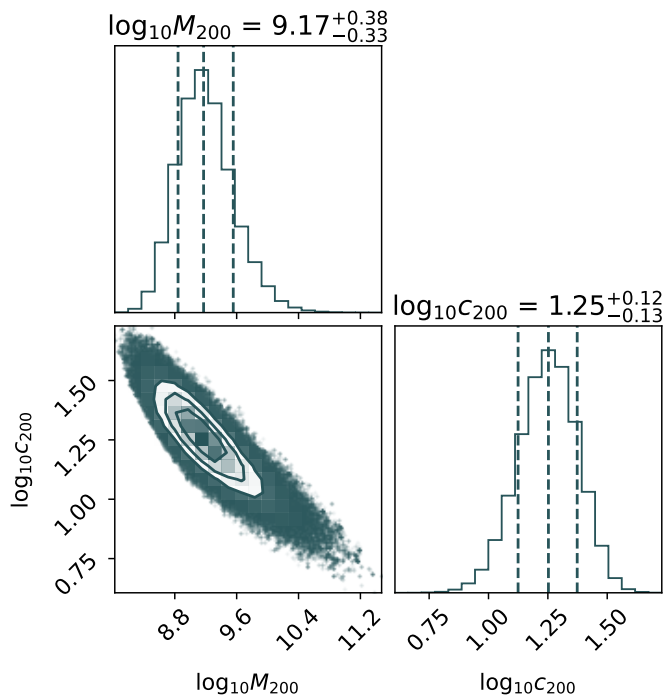


Fig. 5. Constraints on the CDM profile for Ant B. The histograms along the diagonal represent the posterior distribution for each parameter: the virial mass M_{200} in M_{\odot} and the concentration parameter c_{200} . Their units were omitted for clarity. The vertical dashed lines indicate the median and 68% confidence interval. The bottom left panel represents the 2D posterior distribution of these parameters, with the contours corresponding to 0.5σ , 1σ , 1.5σ and 2σ confidence levels, where σ is the standard deviation of the 2D distribution.

For the CDM profile we find a virial mass of $M_{200} = 10^{9.17^{+0.38}_{-0.33}} \approx 1.48^{+2.29}_{-0.79} \times 10^9 M_{\odot}$ and a concentration parameter of $c_{200} = 10^{1.25^{+0.12}_{-0.13}} \approx 17.78^{+5.66}_{-4.60}$. These values are summarised in Table 4.

For the SFDM profile, we find a virial mass of $M_{200} = 10^{9.22^{+0.40}_{-0.35}} \approx 1.66^{+2.51}_{-0.92} \times 10^9 M_{\odot}$ and a concentration parameter of $c_{200} = 10^{1.24^{+0.13}_{-0.12}} \approx 17.38^{+6.06}_{-4.20}$. Clearly, the SFDM and CDM profile fits are in good agreement for these parameters. We can only present the characteristic length scale of the repulsive SI as an upper limit. The posterior distribution that we get for R_{TF} contains values ($R_{TF} \sim 0.63$ pc) that are smaller than the projected radii of our innermost tracer (1.84 pc), leading to a lack of constraining power at the lower end of the range of R_{TF} . We find R_{TF} (kpc) $< 10^{-0.74} \lesssim 0.18$ at the 68% confidence level and R_{TF} (kpc) $< 10^{-0.14} \lesssim 0.72$ at the 95% confidence level. These values are summarised in Table 4.

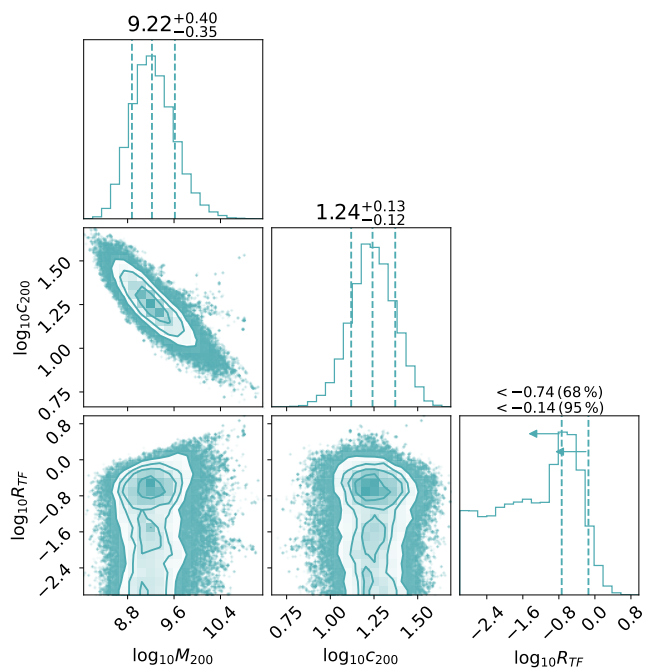


Fig. 6. Constraints on the SFDM profile for Ant B. The histograms along the diagonal represent the posterior distribution for each parameter: the virial mass M_{200} in M_{\odot} , the concentration parameter c_{200} , and the characteristic length scale of the repulsive self-interaction R_{TF} in kpc. Their units were omitted for clarity. The vertical dashed lines indicate the median and 68% confidence interval (without arrows) or the 68% and 95% confidence limits (upper and lower arrows, respectively). The other panels represent the 2D posterior distributions of these parameters, with the contours corresponding to 0.5σ , 1σ , 1.5σ and 2σ confidence levels, where σ is the standard deviation of the 2D distribution.

4.2. Comparison between profiles

The density profiles were generated by drawing 1000 random samples from the remaining samples after the cut was performed on χ^2 . In Figure 7 we show the recovered density profiles for the three models adopted as a function of the radius. These density profiles are represented by the median density of the random samples and their 68% confidence interval at every radius.

The SFDM model agrees with the CDM model within the uncertainties and their agreement is almost perfect at large radii. The uncertainties of the SFDM allow for the CDM model even at the smallest radii, when $R_{TF} \rightarrow 0$. Not surprisingly, the agreement of the discussed models is best at those radii where the density of stars in our sample is highest.

The model that represents cold dark matter has the highest density and smallest uncertainties, while the SFDM model seems to prefer lower densities. However, the density estimates for SFDM are likely biased towards lower values because there is a physical limit set by CDM and the model only allows for that or lower values.

In Table 4 we present the Bayesian evidence Z for both models and the decimal logarithm of the Bayes factor, $\Delta \log_{10}(Z)$, computed concerning the model with the largest Z . This estimation follows the one described in Zoutendijk et al. (2021a,b), and we use MCEVIDENCE (Heavens et al. 2017) for this purpose. We assume the prior probabilities of the models are equal and we take into account that these models have different degrees of freedom. We can compare the models by estimating the ratio of Z , with the model with the largest Z being favoured. According

Table 4. Summary of the Bayesian evidence for CDM and SFDM, as well as the marginalised posterior estimates obtained for the free parameters for both models.

Model	$\log_{10}(Z)$	$\Delta \log_{10}(Z)$	Parameter	Median	2.5%	16%	84%	97.5%
CDM	-124.83	0.00	$M_{200}/(10^9 M_{\odot})$	1.48	1.12	0.79	2.29	8.75
			c_{200}	17.78	8.01	4.60	5.66	12.42
SFDM	-125.49	-0.66	$M_{200}/(10^9 M_{\odot})$	1.66	1.28	0.92	2.51	9.82
			c_{200}	17.38	7.60	4.20	6.06	13.52
			R_{TF} (pc)				$\lesssim 180$	$\lesssim 720$

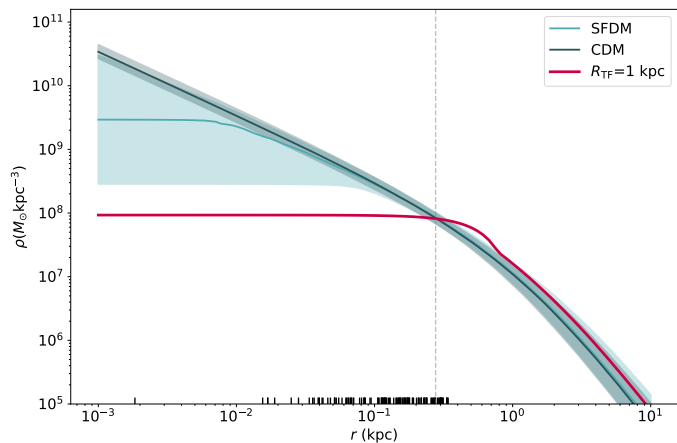


Fig. 7. Recovered DM density profiles of Ant B for the adopted models. The solid lines represent the median density profile: in dark-blue the CDM model is represented and in light blue the SFDM model. The filled areas represent the 68% confidence interval. The solid red line represents the shape of the same density profile if $R_{\text{TF}} = 1$ kpc. The vertical dashed line indicates the half-light radius and the bottom marks represent the projected radii of the members of Ant B.

to the scale of Jeffreys (1961), to completely rule out a model, an odds ratio of 10^{-2} is required. The CDM profile has the largest Bayesian evidence and the Bayes factors indicate that the preference of CDM over SFDM is substantial ($Z < 10^{-0.66}$). However, is still far from significant, and we cannot decisively rule it out.

4.3. Velocity anisotropy profile

Collins et al. (2021) argue that we can use tighter priors on the symmetrised velocity anisotropy $\tilde{\beta}(r)$ since dynamical systems in pseudo-equilibrium, theoretically, should have an isotropic distribution close to the centre with radial or weak tangential anisotropy at large radii (see e.g. Read et al. 2006, Pontzen et al. 2015, Alvey et al. 2020, Orkney et al. 2021). Accordingly, they used $\tilde{\beta}(r) > -0.1$ and $\tilde{\beta}(r) \rightarrow 0$ for $r \rightarrow 0$ as default values in the most recent version of GRAVSPHERE. However, when we first used these priors on the anisotropy profile, the values obtained for the density and mass profile were extremely low. For this reason, we decided to allow the full range of values on $\tilde{\beta}(r)$. We then found out that Ant B prefers a negative anisotropy over all radii, although it becomes more positive for larger radii. This behaviour can be seen in Figure 8. Since all models followed a similar behaviour in the anisotropy profile, the CDM profile was chosen for display, for it is the standard model and proved to be representative of all tested models. The corner plots of the relevant

anisotropy parameters for both models are shown in Figure B.1 of the Appendix.

Given the preference for a tangential anisotropy, we also ran the models with tighter priors on the anisotropy parameters, but this time allowing only for negative values, with $-0.6 < \tilde{\beta}_0 < 0.4$ and $-0.6 < \tilde{\beta}_{\infty} < -0.4$. We get reasonable density profiles for both models but the velocity dispersion is not properly fitted, which suggests that Antlia B does not have a constant anisotropy profile, and therefore we need to allow for the full range for these parameters.

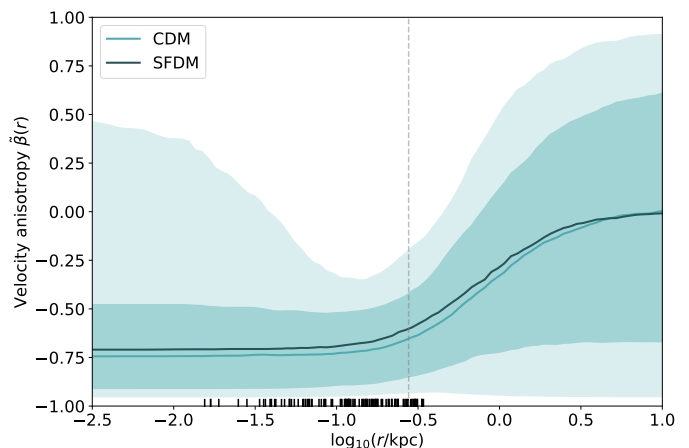


Fig. 8. Velocity anisotropy of Ant B. The best fit from GRAVSPHERE of the symmetrised anisotropy $\tilde{\beta}$ for the CDM model is shown as a solid light blue line, with the light blue shaded regions showing the 68% and 95% confidence intervals for the CDM model. The solid dark blue line represents the best fit for the SFDM model. Since the best fit for both models is so similar, the confidence intervals for the SFDM model are omitted for clarity. The half-light radius is represented by the vertical dashed line and the bottom marks represent the projected radii of the members of Ant B.

The anisotropy profile of this dwarf favours tangential anisotropy in its centre and becomes isotropic - and possibly radial - after the half-right radius. As mentioned, this behaviour is not expected for a system like Ant B, since it is thought that this galaxy is in pseudo-equilibrium. The reason behind this feature can be due to several reasons, ranging from tidal interaction with its host galaxy, a gas disk formed before its stars, unmodelled rotation, or even the presence of a star cluster contaminating the inner bin. We will discuss the astrophysical implications and investigate the origin of this result in a companion paper (Brinchmann et al. in prep). The impact that this feature has on the dark matter constraints will be discussed in Sect. 5.2.

5. Discussion

The virial mass $M_{200} \sim 10^9 M_\odot$ and the concentration parameter c_{200} found for this system using both the CDM and the SFDM model are consistent with it being a gas-rich ultra-faint like Leo T (Vaz et al. submitted). The implications of our findings for galaxy formation models will also be discussed in detail in Brinchmann et al. in prep; see also Zoutendijk et al. 2021b).

5.1. Constraints on the dark matter models

Turning now to the dark matter constraints that we were able to obtain, to match the observations of dwarf galaxies in the Local Group that show cores of the size ~ 1 kpc, the SI strength parameter has to satisfy $R_{\text{TF}} \sim 1$ kpc $\iff \frac{g}{m^2 c^4} \lesssim 2 \times 10^{-18} \text{ eV}^{-1} \text{ cm}^3$. Furthermore, Li et al. (2014, 2017) were able to place upper limits on the values of m and g based on observational consequences while assuming that dark matter is SFDM. They took into account all the phases in the evolution of the Universe and how the value of g/m^2 would influence the duration of these different phases. The redshift required by the observations of the CMB temperature anisotropy power spectrum for the transition from a radiation-dominated to a matter-dominated Universe places an upper limit for g/m^2 of $\frac{g}{m^2 c^4} \lesssim 4 \times 10^{-17} \text{ eV}^{-1} \text{ cm}^3$, corresponding to $R_{\text{TF}} \leq 5$ kpc. Additionally, Dawoodbhoy et al. (2021) were able to get an estimate of the minimum particle mass to ensure that for the SFDM-TF regime, $R_{\text{TF}} \gg \lambda_{\text{deB}}$, given by

$$\frac{mc^2}{10^{-21} \text{ eV}} \gg \left(\frac{M_{200,\text{min}}}{10^9 M_\odot} \right)^{-1/3} \left(\frac{R_{\text{TF}}}{1 \text{ kpc}} \right)^{-1}, \quad (12)$$

where $M_{200,\text{min}}$ is the minimum halo mass that needs to be accommodated by the model.

Our upper limit on the characteristic length scale is $R_{\text{TF}} \lesssim 0.18$ kpc at the 68% confidence level and $R_{\text{TF}} \lesssim 0.72$ kpc at the 95% confidence level, which translates to $\frac{g}{m^2 c^4} \lesssim 5.2 \times 10^{-20} \text{ eV}^{-1} \text{ cm}^3$ at the 68% confidence level and $\frac{g}{m^2 c^4} \lesssim 8.3 \times 10^{-20} \text{ eV}^{-1} \text{ cm}^3$ at the 95% confidence level. Using these values we can also determine the minimum particle mass $m \gg 4.8 \times 10^{-21} \text{ eV}/c^2$. To give a visual illustration of the tension between the R_{TF} required by Dawoodbhoy et al. (2021) and what we find, Figure 7 also contains a density profile for Antlia B with $R_{\text{TF}} = 1$ kpc, assuming that M_{200} and c_{200} have the median values found for SFDM above. As is clear, the required density profile is strongly inconsistent with the one we find. In Figure 4 we also show the shape that the velocity dispersion of Antlia B would have if $R_{\text{TF}} = 1$ kpc, assuming that the free parameters of the SFDM have the same median values previously found.

The lack of line-of-sight velocities for stars very close to the centre limits our ability to constrain the density profile below 30 pc (check Figure 7) and this limits our ability to place stronger constraints on SFDM.

More recently, Shapiro et al. (2021) revisited structure formation in the SFDM in the cosmological context to understand if the requirement of $R_{\text{TF}} \gtrsim 1$ kpc was consistent with the cosmological formation of these haloes. To do this, they applied the equations previously derived in Dawoodbhoy et al. (2021) to simulate individual halo formation by spherical infall and collapse in a cosmologically expanding universe. Using CDM-like initial conditions, they found that the density profiles were similar to those found using non-cosmological initial conditions, being consistent with the former requirement of $R_{\text{TF}} \gtrsim 1$ kpc. However, the initial conditions for SFDM halo formation may differ from those for CDM. To overcome this, they used linear

perturbation theory to estimate the range of R_{TF} -values which are consistent with observational constraints on the Fuzzy Dark Matter model. In this case, a core as large as $R_{\text{TF}} \gtrsim 1$ kpc is disfavoured. To match the FDM particle masses $1 \times 10^{-22} \lesssim m$ ($\text{eV} c^{-2}$) $\lesssim 30 \times 10^{-22}$, a core of $10 \gtrsim R_{\text{TF}}$ (pc) $\gtrsim 1$ is required, favouring sub-kpc core sizes. However, in this range, SFDM approaches CDM, and the problems associated with the standard model start to arise once again. This suggests that either the observational constraints of FDM cannot be used to place the corresponding constraints on the core sizes of the haloes formed in SFDM, or SFDM is an incompatible explanation for the observed cores in the dwarfs of the Local Group. In Hartman et al. (2022) and Hartman et al. (2022), similar conclusions were drawn, using large-scale observables and fully 3D cosmological simulations, respectively.

5.2. Testing the robustness of the results

The centre measured by Sand et al. (2015) might be miscalculated since there is a bright star close to it, partially overlapping the galaxy. To test the robustness of the results, we started by changing the centre of Ant B by ($\alpha \sim 1''$, $\delta \sim 3''$) to see how much our results would be affected. We rerun BINULATOR and GRAVSPHERE on both models for Ant B with the new centre. The velocity dispersion for each bin, the recovered velocity dispersion profile and the anisotropy profile associated with the new centre can be seen in Figures C.1, C.2 and C.3 of the Appendix, respectively. Figures C.4 and C.5 show the new parameters derived for these profiles. We find a virial mass of $M_{200} \approx 1.29_{-0.71}^{+2.02} \times 10^9 M_\odot$ and a concentration parameter of $c_{200} \approx 18.20_{-4.71}^{+5.79}$ for the CDM model and $M_{200} \approx 1.35_{-0.76}^{+2.04} \times 10^9 M_\odot$ and $c_{200} \approx 17.78_{-4.60}^{+5.66}$ for the SFDM model. We find $R_{\text{TF}} \lesssim 0.11$ kpc at the 68% confidence level and $R_{\text{TF}} \lesssim 0.68$ kpc at the 95% confidence level. Let us notice that this time we run the code with half the steps to make the process faster since we solely wanted to check whether our results were not dramatically affected by changing the centre. These results are very close to those previously obtained. This is as expected since the innermost bin after radial binning still contains 20 of the 25 stars that we have with the nominal centre.

We find that Ant B favours tangential inner velocity anisotropy for both the CDM and SFDM model. We will discuss the interpretation of these results and implications for galaxy formation models in a companion paper (Brinchmann et al. in prep). Since the anisotropy has its lowest value in the centre of the galaxy, we need to test whether the constraints on the dark matter parameters are affected when we remove the stars that are, in principle, responsible for this behaviour. To do this, we remove the 25 stars closest to the centre that correspond to the first bin (represented in Figure 4). We rerun BINULATOR and GRAVSPHERE on both models for Ant B without these 25 stars. The velocity dispersion for each bin, the recovered velocity dispersion profile and the anisotropy profile associated with the new centre can be seen in Figures C.6, C.7 and C.8 of the Appendix, respectively.

As can be seen in Figure C.9, the parameters of the CDM model suffer almost no changes: we find a virial mass of $M_{200} \approx 1.55_{-0.98}^{+3.24} \times 10^9 M_\odot$ and a concentration parameter of $c_{200} \approx 17.38_{-4.50}^{+6.06}$. In Figure C.10 it is possible to see how the dark matter constraints for SFDM changed with the removal of the innermost bin. Looking at the physical constraints on R_{TF} , we find a lower value at the 68% confidence level ($R_{\text{TF}} \lesssim 0.11$ kpc instead of $\lesssim 0.18$ kpc) and a slightly higher value at the 95% confidence level ($R_{\text{TF}} \lesssim 0.81$ kpc instead of $\lesssim 0.72$ kpc). Sim-

ilarly to what was done in the previous robustness test, we run the code with half the steps.

The parameters associated with the anisotropy profile continue to show the same behaviour as before: the anisotropy is tangential in the centre of the galaxy and becomes almost isotropic when we approach larger radii (Figure C.8). However, this tangential anisotropy becomes less statistically significant by removing the innermost bin (Figure C.11). Since we find that the recovered SFDM model parameters do not change significantly, we consider our SFDM profile results robust.

6. Conclusions

In this work, we present the first spectroscopic observations of Antlia B, a distant dwarf found by Sand et al. (2015). With them, we were able to determine kinematic data, previously presented by Zoutendijk et al. (2021b), and ensure the membership of 127 stars. These observations allowed us to determine the intrinsic mean line-of-sight velocity $v_{\text{LOS}} = 375.39^{+0.98}_{-0.97}$ km s⁻¹ and the velocity dispersion $\sigma_{v_{\text{LOS}}} = 7.87^{+1.02}_{-0.98}$ km s⁻¹ of this galaxy. The estimated v_{LOS} is in agreement with the velocity of H I gas present in this galaxy ($v_{\text{HI}} \sim 375$ km s⁻¹).

The kinematic data of Ant B also allowed us to derive the dark matter density profiles for this dwarf. From them we were able to determine the virial mass $M_{200} \approx 10^{9.2} M_{\odot}$ and the concentration parameter $c_{200} \approx 17$ of Ant B. The values found for these parameters for both dark matter models are consistent with the values expected from models in which the smallest dwarf galaxies are reionization fossils.

We found that Ant B favours tangential anisotropy in its centre, although it becomes more positive for larger radii, showing an isotropic behaviour - and possibly radial - after the half-right radius.

We find substantial Bayesian evidence ($Z < 10^{-0.66}$) against the SFDM model. However, it is not significant, and we cannot completely rule out this model solely based on this result.

We constrained the characteristic length scale of the repulsive self-interaction R_{TF} of the SFDM model of $R_{\text{TF}} \lesssim 180$ pc (68% confidence level) and $R_{\text{TF}} \lesssim 720$ pc (95% confidence level), which translates to $\frac{g}{m^2 c^4} \lesssim 5.2 \times 10^{-20}$ eV⁻¹ cm³ (68% confidence level) and $\frac{g}{m^2 c^4} \lesssim 8.3 \times 10^{-20}$ eV⁻¹ cm³ (95% confidence level). This gives us a minimum particle mass of $m \gg 4.8 \times 10^{-21}$ eV/c². Though we cannot rule SFDM entirely, we find a constraint on R_{TF} that rules out that it is a solution to the core-cusp problem.

Tests show that the derived constraints are robust against different model assumptions, such as changing the location of the centre or removing the stars closest to it, with minimal impact on the final results.

The R_{TF} that we found is not large enough to solve the core-cusp problem and therefore this model cannot explain cores in dwarfs in the Local Group.

To further improve the constraints placed on the SFDM model, line-of-sight velocities of stars closer to the centre would be required. This remains challenging since not only Ant B is a distant and faint system, but it also has a bright foreground star partially overlapping this galaxy.

The dark matter density profiles of ultra-faint dwarfs have only started to be estimated very recently. The measurements of the velocity of stars of these galaxies with the spectroscopic data from MUSE-Faint allow us to improve the constraints on their inner dark matter density profiles. With a larger number of UFDs analysed, we will be able to place stronger constraints on

the physical properties of dark matter. Furthermore, we want to additionally explore other alternative dark matter models, that will take us one step closer to understanding this unknown form of matter.

Acknowledgements. We thank the anonymous referee for their helpful comments, which improved the manuscript. MPJ thanks Marcel S. Pawlowski, Pengfei Li, Salvatore Taibi and Jamie K. Kanehisa for the valuable discussions and advice. MPJ and JB acknowledge support by Fundação para a Ciência e a Tecnologia (FCT) through the research grants UID/FIS/04434/2019, UIDB/04434/2020, UIDP/04434/2020 and PTDC/FIS-AST/4862/2020. JB acknowledges support from FCT work contract 2020.03379.CEECIND. SLZ acknowledges support by The Netherlands Organisation for Scientific Research (NWO) through a TOP Grant Module 1 under project number 614.001.652. SKA acknowledges funding from UKRI in the form of a Future Leaders Fellowship (grant number MR/T022868/1). Based on observations made with ESO Telescopes at the La Silla Paranal Observatory under programme IDs 0100.D-0807, 0101.D-0300, 0102.D-0372 and 0103.D-0705. This research has made use of Astropy (Astropy Collaboration et al. 2018), corner.py (Foreman-Mackey 2016), matplotlib (Hunter 2007), NASA's Astrophysics Data System Bibliographic Services, NumPy (Harris et al. 2020), SciPy (Virtanen et al. 2020). Based on observations made with the NASA/ESA Hubble Space Telescope, and obtained from the Hubble Legacy Archive, which is a collaboration between the Space Telescope Science Institute (STScI/NASA), the Space Telescope European Coordinating Facility (ST-ECF/ESA) and the Canadian Astronomy Data Centre (CADNRC/CSA).

References

- Alvey, J., Sabti, N., Tiki, V., et al. 2020, *Monthly Notices of the Royal Astronomical Society*, 501, 1188–1201
- Astropy Collaboration, Price-Whelan, A. M., Sipőcz, B. M., et al. 2018, *AJ*, 156, 123
- Bacon, R., Accardo, M., Adjali, L., et al. 2010, in *SPIE Proceedings*, ed. I. S. McLean, S. K. Ramsay, & H. Takami (SPIE)
- Bacon, R., Conseil, S., Mary, D., et al. 2017, *A&A*, 608, A1
- Baur, J., Palanque-Defabrouille, N., Yè che, C., Magneville, C., & Viel, M. 2016, *Journal of Cosmology and Astroparticle Physics*, 2016, 012
- Berezhiani, L. & Khoury, J. 2015, *Phys. Rev. D*, 92, 103510
- Bertin, E. & Arnouts, S. 1996, *A&AS*, 117, 393–404
- Bertone, G. & Hooper, D. 2018, *Reviews of Modern Physics*, 90
- Bettoni, D., Colombo, M., & Liberati, S. 2014, *Journal of Cosmology and Astroparticle Physics*, 2014, 004
- Bosma, A. 1981, *AJ*, 86, 1825–1846
- Bovill, M. S. & Ricotti, M. 2011, *The Astrophysical Journal*, 741, 17
- Boylan-Kolchin, M., Bullock, J. S., & Kaplinghat, M. 2011, *MNRAS*, 415, L40–L44
- Bozek, B., Fitts, A., Boylan-Kolchin, M., et al. 2018, *Monthly Notices of the Royal Astronomical Society*, 483, 4086–4099
- Bressan, A., Marigo, P., Girardi, L., et al. 2012, *Monthly Notices of the Royal Astronomical Society*, 427, 127–145
- Bullock, J. S. & Boylan-Kolchin, M. 2017, *Annual Review of Astronomy and Astrophysics*, 55, 343–387
- Calabrese, E. & Spergel, D. N. 2016, *Monthly Notices of the Royal Astronomical Society*, 460, 4397–4402
- Carlson, E. D., Machacek, M. E., & Hall, L. J. 1992, *ApJ*, 398, 43
- Clifton, T., Ferreira, P. G., Padilla, A., & Skordis, C. 2012, *Physics Reports*, 513, 1–189, modified Gravity and Cosmology
- Clowe, D., Bradač, M., Gonzalez, A. H., et al. 2006, *ApJ*, 648, L109–L113
- Collins, M. L. M. & Read, J. I. 2022, *Nature Astronomy*, 6, 647–658
- Collins, M. L. M., Read, J. I., Ibata, R. A., et al. 2021, *Monthly Notices of the Royal Astronomical Society*, 505, 5686–5701
- Dawoodbhoj, T., Shapiro, P. R., & Rindler-Daller, T. 2021, *Monthly Notices of the Royal Astronomical Society*, 506, 2418–2444
- de Blok, W. J. G. 2010, *Advances in Astronomy*, 2010, 789293
- Dine, M. & Fischler, W. 1983, *Physics Letters B*, 120, 137–141
- Dodelson, S. 2011, *International Journal of Modern Physics D*, 20, 2749–2753
- El-Zant, A., Shlosman, I., & Hoffman, Y. 2001, *The Astrophysical Journal*, 560, 636–643
- Errani, R., Peñarrubia, J., & Walker, M. G. 2018, *Monthly Notices of the Royal Astronomical Society*, 481, 5073–5090
- Ferreira, E. G. M. 2021, *A&A Rev.*, 29, 7
- Finkelstein, S. L., D'Aloisio, A., Paardekooper, J.-P., et al. 2019, *The Astrophysical Journal*, 879, 36, publisher: The American Astronomical Society
- Flores, R. A. & Primack, J. R. 1994, *The Astrophysical Journal*, 427, L1
- Foreman-Mackey, D. 2016, *The Journal of Open Source Software*, 1, 24

- Foreman-Mackey, D., Hogg, D. W., Lang, D., & Goodman, J. 2013, *Publications of the Astronomical Society of the Pacific*, 125, 306–312
- Genina, A., Read, J. I., Frenk, C. S., et al. 2020, *MNRAS*, 498, 144–163
- Gilman, D., Du, X., Benson, A., et al. 2019, *Monthly Notices of the Royal Astronomical Society: Letters*, 492, L12–L16
- Griest, K. 1991, *ApJ*, 366, 412
- Hargis, J. R., Albers, S., Crnojević, D., et al. 2020, *ApJ*, 888, 31
- Hargreaves, J. C., Gilmore, G., Irwin, M. J., & Carter, D. 1994, *MNRAS*, 269, 957–974
- Harris, C. R., Millman, K. J., van der Walt, S. J., et al. 2020, *Nature*, 585, 357–362
- Hartman, S., Winther, H., & Mota, D. 2022, *Journal of Cosmology and Astroparticle Physics*, 2022, 005
- Hartman, S. T. H., Winther, H. A., & Mota, D. F. 2022, *A&A*, 666, A95
- Harvey, D., Massey, R., Kitching, T., Taylor, A., & Tittley, E. 2015, *Science*, 347, 1462–1465
- Hawking, S. 1971, *MNRAS*, 152, 75
- Heavens, A., Fantaye, Y., Mootooyaloo, A., et al. 2017, arXiv e-prints, arXiv:1704.03472
- Hu, W., Barkana, R., & Gruzinov, A. 2000, *Phys. Rev. Lett.*, 85, 1158–1161
- Hui, L., Ostriker, J. P., Tremaine, S., & Witten, E. 2017, *Physical Review D*, 95
- Hunter, J. D. 2007, *Computing in Science and Engineering*, 9, 90–95
- Husser, T.-O. 2012, *3D-Spectroscopy of Dense Stellar Populations* (Göttingen: Universitätsverlag Göttingen)
- Husser, T.-O., Kamann, S., Dreizler, S., et al. 2016, *A&A*, 588, A148
- Husser, T.-O., Wende-von Berg, S., Dreizler, S., et al. 2013, *A&A*, 553, A6
- Ibata, R., Sollima, A., Nipoti, C., et al. 2011, *ApJ*, 738, 186
- Jean, J. H. 1922, *Monthly Notices of the Royal Astronomical Society*, 82, 122–132
- Jeffreys, H. 1961, *Theory of Probability*, International series of monographs on physics (Clarendon Press)
- Kamann, S., Husser, T. O., Brinchmann, J., et al. 2016, *A&A*, 588, A149
- Kamann, S., Wisotzki, L., & Roth, M. M. 2013, *A&A*, 549, A71
- Kaplinghat, M., Knox, L., & Turner, M. S. 2000, *Physical Review Letters*, 85, 3335–3338
- Klypin, A., Kravtsov, A. V., Valenzuela, O., & Prada, F. 1999, *ApJ*, 522, 82–92
- Lee, J. & Koh, I. 1996, *Phys. Rev. D*, 53, 2236–2239
- Li, B., Rindler-Daller, T., & Shapiro, P. R. 2014, *Phys. Rev. D*, 89, 083536
- Li, B., Shapiro, P. R., & Rindler-Daller, T. 2017, *Phys. Rev. D*, 96, 063505
- Martin, N. F., Collins, M. L. M., Longeard, N., & Tollerud, E. 2018, *ApJ*, 859, L5
- Massey, R., Harvey, D., Liesenborgs, J., et al. 2018, *MNRAS*, 477, 669–677
- Matos, T., Guzmán, F. S., & Ureña-López, L. A. 2000, *Classical and Quantum Gravity*, 17, 1707–1712
- Merrifield, M. R. & Kent, S. M. 1990, *AJ*, 99, 1548
- Moore, B. 1994, *Nature*, 370, 629–631
- Moore, B., Ghigna, S., Governato, F., et al. 1999, *The Astrophysical Journal*, 524, L19–L22
- Natarajan, P. & Zhao, H. 2008, *MNRAS*, 389, 250–256
- Navarro, J. F., Eke, V. R., & Frenk, C. S. 1996, *MNRAS*, 283, L72–L78
- Navarro, J. F., Frenk, C. S., & White, S. D. M. 1996, *The Astrophysical Journal*, 462, 563
- Nipoti, C. & Binney, J. 2014, *Monthly Notices of the Royal Astronomical Society*, 446, 1820–1828
- Oman, K. A., Navarro, J. F., Fattahi, A., et al. 2015, *MNRAS*, 452, 3650–3665
- Orkney, M. D. A., Read, J. I., Rey, M. P., et al. 2021, *Monthly Notices of the Royal Astronomical Society*, 504, 3509–3522
- Peebles, P. J. E. 2000, *ApJ*, 534, L127–L129
- Peñarrubia, J., Pontzen, A., Walker, M. G., & Kroupa, S. E. 2012, *The Astrophysical Journal*, 759, L42
- Planck Collaboration, Ade, P. A. R., Aghanim, N., et al. 2016, *A&A*, 594, A13
- Plummer, H. C. 1911, *Monthly Notices of the Royal Astronomical Society*, 71, 460
- Pontzen, A., Read, J. I., Teyssier, R., et al. 2015, *MNRAS*, 451, 1366–1379
- Preskill, J., Wise, M. B., & Wilczek, F. 1983, *Physics Letters B*, 120, 127–132
- Read, J. I. & Erkal, D. 2019, *MNRAS*, 487, 5799–5812
- Read, J. I. & Steger, P. 2017, *Monthly Notices of the Royal Astronomical Society*, 471, 4541–4558
- Read, J. I., Walker, M. G., & Steger, P. 2018, *Monthly Notices of the Royal Astronomical Society*, 481, 860–877
- Read, J. I., Walker, M. G., & Steger, P. 2019, *MNRAS*, 484, 1401–1420
- Read, J. I., Wilkinson, M. I., Evans, N. W., Gilmore, G., & Klypin, A. 2006, *MNRAS*, 367, 387–399
- Rindler-Daller, T. & Shapiro, P. R. 2012, *Monthly Notices of the Royal Astronomical Society*, 422, 135–161
- Roth, M. M., Sandin, C., Kamann, S., et al. 2018, *A&A*, 618, A3
- Rubin, V. C., Ford, W. K., J., & Thonnard, N. 1980, *ApJ*, 238, 471–487
- Sand, D. J., Spekkens, K., Crnojević, D., et al. 2015, *Astrophys. J. Lett.*, 812, L13
- Schaye, J., Crain, R. A., Bower, R. G., et al. 2015, *MNRAS*, 446, 521–554
- Shapiro, P. R., Dawoodbhai, T., & Rindler-Daller, T. 2021, arXiv e-prints, arXiv:2106.13244
- Simon, J. D. 2019, *Annual Review of Astronomy and Astrophysics*, 57, 375–415
- Soto, K. T., Lilly, S. J., Bacon, R., Richard, J., & Conseil, S. 2016, ZAP: Zurich Atmosphere Purge, Astrophysics Source Code Library, record ascl:1602.003
- Springel, V., Frenk, C. S., & White, S. D. M. 2006, *Nature*, 440, 1137–1144
- Valenzuela, O., Rhee, G., Klypin, A., et al. 2007, *ApJ*, 657, 773–789
- Virtanen, P., Gommers, R., Oliphant, T. E., et al. 2020, *Nature Methods*, 17, 261–272
- Vogelsberger, M., Genel, S., Springel, V., et al. 2014, *Monthly Notices of the Royal Astronomical Society*, 444, 1518–1547
- Weilbacher, P. M., Palsa, R., Streicher, O., et al. 2020, *A&A*, 641, A28
- Wheeler, C., Oñorbe, J., Bullock, J. S., et al. 2015, *Monthly Notices of the Royal Astronomical Society*, 453, 1305–1316
- Willman, B. & Strader, J. 2012, *AJ*, 144, 76
- Zoutendijk, S. L., Brinchmann, J., Boogaard, L. A., et al. 2020, *A&A*, 635, A107
- Zoutendijk, S. L., Brinchmann, J., Bouché, N. F., et al. 2021a, *Astronomy & Astrophysics*, 651, A80
- Zoutendijk, S. L., Júlio, M. P., Brinchmann, J., et al. 2021b, arXiv e-prints, arXiv:2112.09374
- Zwicky, F. 1933, *Helvetica Physica Acta*, 6, 110–127

Appendix A: Numerical parametrization of SFDM

The estimation of the SFDM model is not trivial, since to determine α and ρ_c for a given halo to obtain the density profile, one has to ensure continuity in the density profile and mass conservation at the switch point (Dawoodbhoy et al. 2021), described, respectively, by

$$\rho_c \operatorname{sinc}(\pi\alpha) = \rho_{\text{CDM}}(\alpha R_{\text{TF}}) \quad (\text{A.1})$$

and

$$\int_0^{\alpha R_{\text{TF}}} \rho_c \operatorname{sinc}\left(\frac{\pi r}{R_{\text{TF}}}\right) 4\pi r^2 dr = \int_0^{\alpha R_{\text{TF}}} \rho_{\text{CDM}}(r) 4\pi r^2 dr. \quad (\text{A.2})$$

Integrating both sides of Equation A.2, we get

$$\frac{4}{\pi^2} R_{\text{TF}}^3 \rho_c (\pi\alpha \cos(\pi\alpha) - \sin(\pi\alpha)) + 4\pi\rho_0 r_s^3 \left[\ln\left(\frac{r_s + \alpha R_{\text{TF}}}{r_s}\right) + \frac{r_s}{r_s + \alpha R_{\text{TF}}} - 1 \right] = 0. \quad (\text{A.3})$$

Now, we can uncouple the unknown parameters α and ρ_c . Equation A.1 can be written as

$$\rho_c = \frac{\pi\alpha}{\sin(\pi\alpha)} \cdot \frac{\rho_0}{\alpha R_{\text{TF}}/r_s(1 + \alpha R_{\text{TF}}/r_s)^2}. \quad (\text{A.4})$$

Thus, Equation A.3 loses its dependence in ρ_c , allowing us to solve it for α

$$\pi^2 r_s^3 \left[\ln\left(\frac{r_s + \alpha R_{\text{TF}}}{r_s}\right) + \frac{r_s}{r_s + \alpha R_{\text{TF}}} - 1 \right] - \alpha R_{\text{TF}}^3 \cdot \frac{1 - \pi\alpha \cot(\pi\alpha)}{\alpha R_{\text{TF}}(1 + \alpha R_{\text{TF}}/r_s)^2} = 0. \quad (\text{A.5})$$

The solution of Equation A.5 can be found using a root solver and then ρ_c can be easily computed. However, this equation admits two solutions and one of them leads to a negative ρ_c , which is not a physical solution. For this reason, one has to carefully choose the interval where α leads to positive values of ρ_c . After several tries and an extensive study of this equation, a reasonable range to look for a solution is $0.4 < \alpha < 0.99$. With both α and ρ_c determined, the mass profile can be determined

$$M_{\text{SFDM}}(r) = \begin{cases} 4\pi\rho_c \int_0^r r^2 \operatorname{sinc}(r/R_{\text{TF}}) dr & r \leq \alpha R_{\text{TF}} \\ M_{\text{CDM}} & r \geq \alpha R_{\text{TF}} \end{cases}. \quad (\text{A.6})$$

The density profile is now also easily computed through Equation 6.

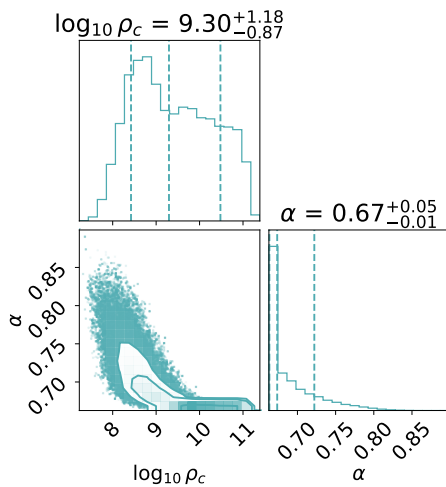


Fig. A.1. Corner plot of the computational parameters α and ρ_c used in the parametrization of the SFDM model.

Appendix B: GRAVSPHERE fits

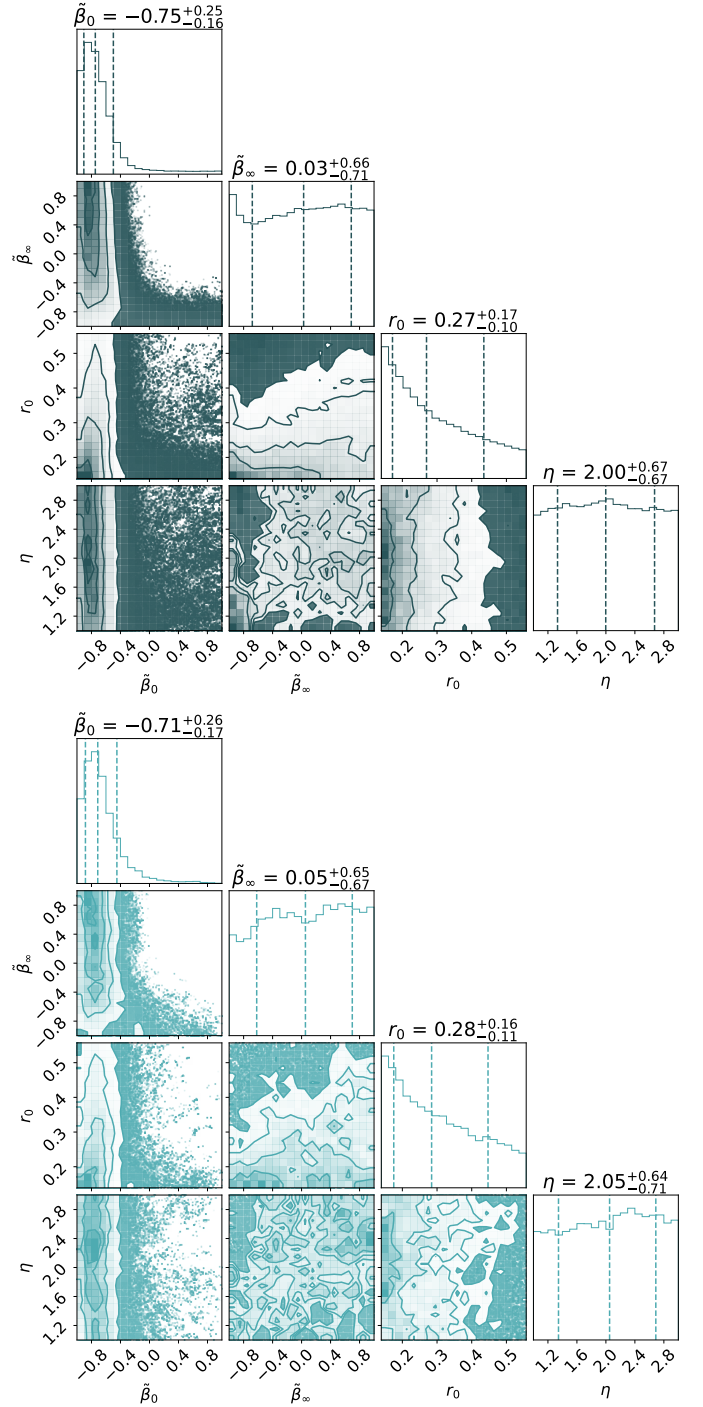


Fig. B.1. **Top:** Corner plot of the parameters $\tilde{\beta}_0$, $\tilde{\beta}_\infty$, r_0 and η of the anisotropy profile for the CDM. **Bottom:** Corner plot of the parameters $\tilde{\beta}_0$, $\tilde{\beta}_\infty$, r_0 and η of the anisotropy profile for the SFDM model.

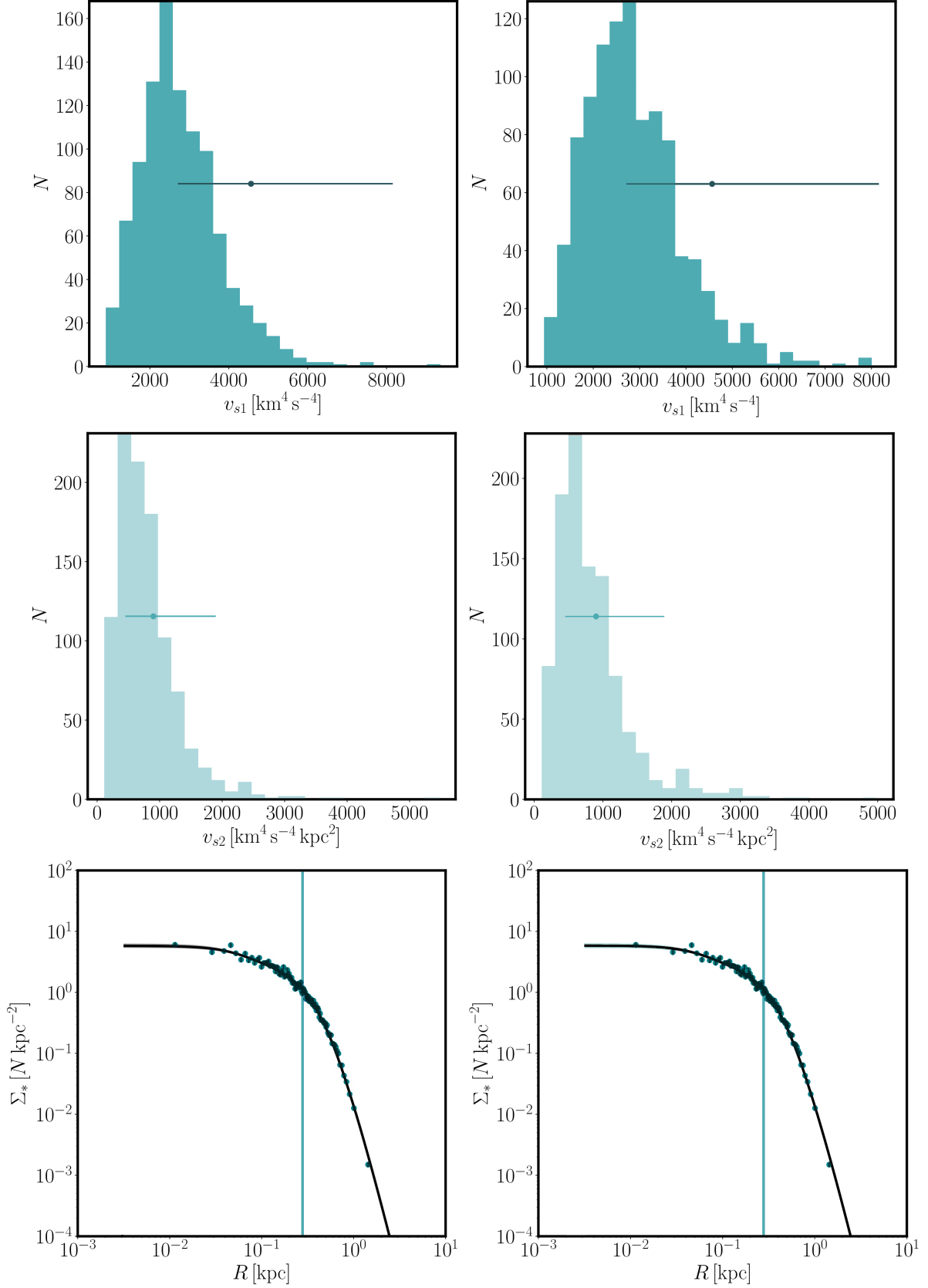


Fig. B.2. Top and centre: Virial Shape Parameters (v_{s1} on top and v_{s2} on centre, for both CDM model (left) and SFDM right). **Bottom:** The surface brightness profile Σ_* for Ant B. The blue points show the photometric data. The best fit from GRAVSPHERE is shown as a solid black line, with the grey shaded regions showing the 68% and 95% confidence intervals for the CDM model (right) and the SFDM model (left).

Appendix C: Robustness of the constraints

C.1. Changing the centre

The robustness of the constraints of the SFDM model was analysed in two different tests, explained in detail in Sect. 5.2. The first one consisted in changing the centre of Ant B by ($\alpha \sim 1''$, $\delta \sim 3''$). The velocity dispersion for each bin after this change, the respective recovered velocity dispersion profile, and the anisotropy profile associated with the new centre can be seen in Figures C.1, C.2 and C.3, respectively. The constraints obtained for both the CDM and SFDM profile for Ant B after changing the coordinates of the centre are represented in Figures C.4 and C.5, respectively.

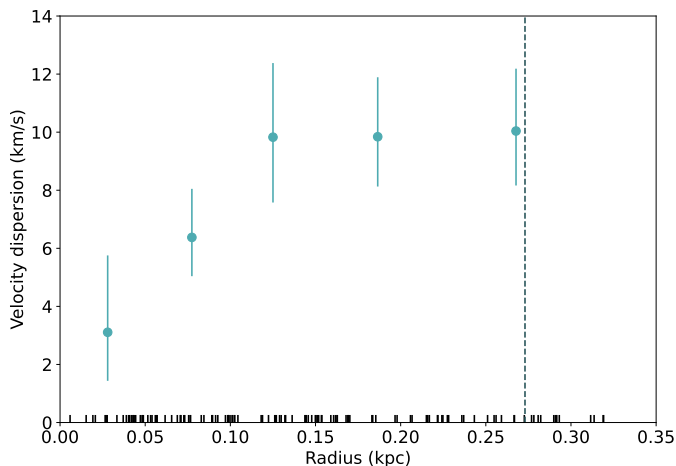


Fig. C.1. Velocity dispersion for each bin with their associated uncertainties after changing the coordinates of the centre of Ant B. The vertical dashed line indicates the half-light radius and the bottom marks represent the projected radii of the members of Ant B.

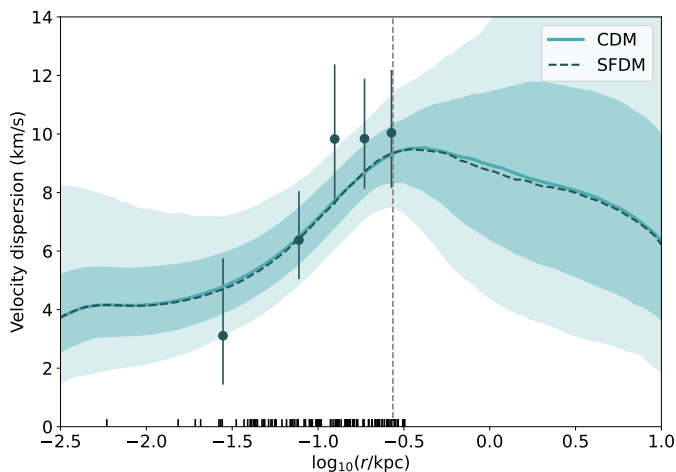


Fig. C.2. Velocity dispersion of Ant B after changing the coordinates of the centre. The dark blue points represent the binned velocity dispersion previously shown. The best fit from GravSphere for the CDM model is shown as a solid light blue line, with the light blue shaded regions showing the 68% and 95% confidence intervals for the CDM model. The dashed dark blue line represents the best fit for the SFDM model. Since the best fit for both models is so similar, the confidence intervals for the SFDM model are omitted for clarity. The half-light radius is represented by the vertical dashed line and the bottom marks represent the projected radii of the members of Ant B.

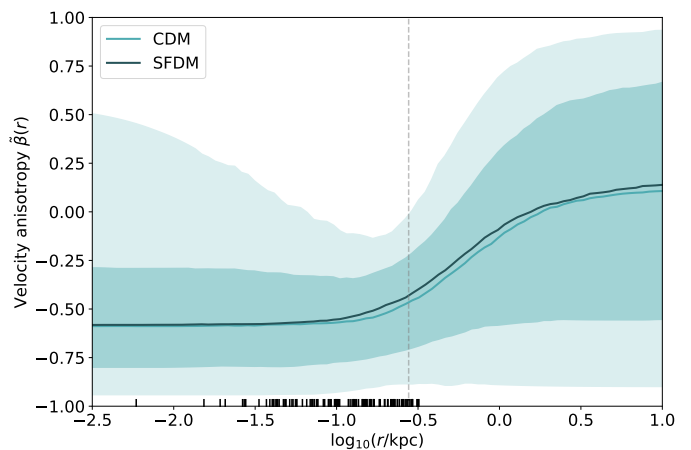


Fig. C.3. Velocity anisotropy profile of Ant B after changing the coordinates of the centre. The best fit from GravSphere of the symmetrised anisotropy β for the CDM model is shown as a solid light blue line, with the light blue shaded regions showing the 68% and 95% confidence intervals for the CDM model. The solid dark blue line represents the best fit for the SFDM model. Since the best fit for both models is so similar, the confidence intervals for the SFDM model are omitted for clarity. The half-light radius is represented by the vertical dashed line and the bottom marks represent the projected radii of the members of Ant B.

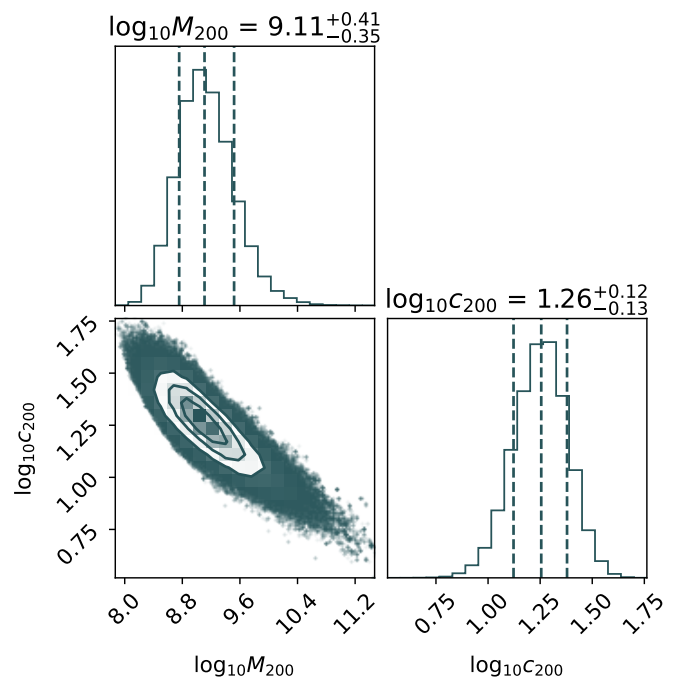


Fig. C.4. Constraints on the CDM profile for Ant B after changing the coordinates of the centre. The histograms along the diagonal represent the posterior distribution for each parameter: the virial mass M_{200} in M_{\odot} and the concentration parameter c_{200} .

C.2. Removing the innermost bin

The second robustness test was motivated by the tangential anisotropy profile found in Ant B. The stars belonging to the first bin were removed since the first bin seemed to be the cause of this behaviour, as can be seen in the data points in Figure 4. The velocity dispersion for each bin after without the innermost bin, the respective recovered velocity dispersion profile, and the anisotropy profile associated can be seen in Figures C.6, C.7

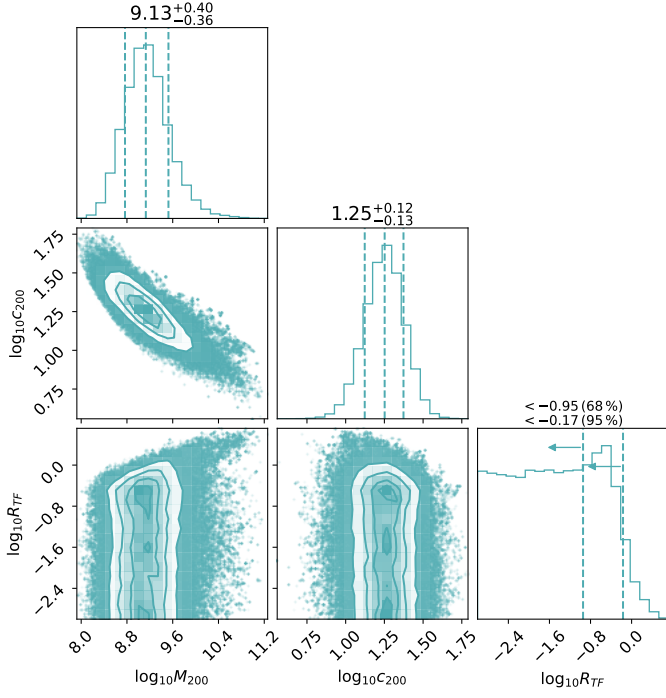


Fig. C.5. Constraints on the SFDM profile for Ant B after changing the coordinates of the centre. The histograms along the diagonal represent the posterior distribution for each parameter: the virial mass M_{200} in M_{\odot} , the concentration parameter c_{200} , and the characteristic length scale of the repulsive self-interaction R_{TF} in kpc.

and C.8, respectively. The constraints obtained for both the CDM and SFDM profile for Ant B after removing the innermost bin are represented in Figures C.9 and C.10, respectively. The posterior distributions obtained for the anisotropy parameters using this configuration can be seen in Figure C.11.

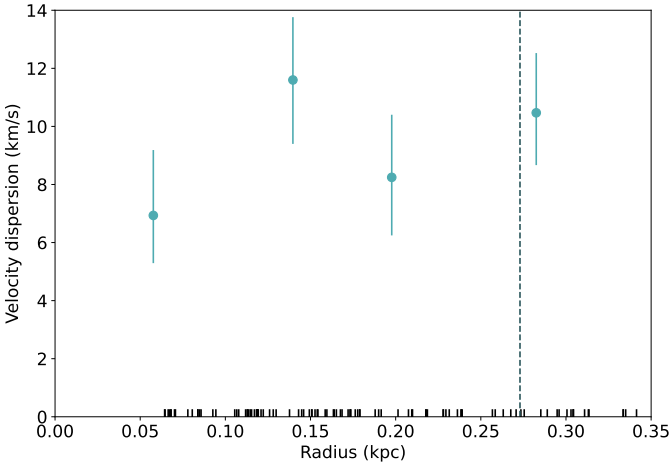


Fig. C.6. Velocity dispersion for each bin with their associated uncertainties for the 102 remaining stars after the cut of the 25 closest to the centre. The vertical dashed line indicates the half-light radius and the bottom marks represent the projected radii of the members of Ant B.

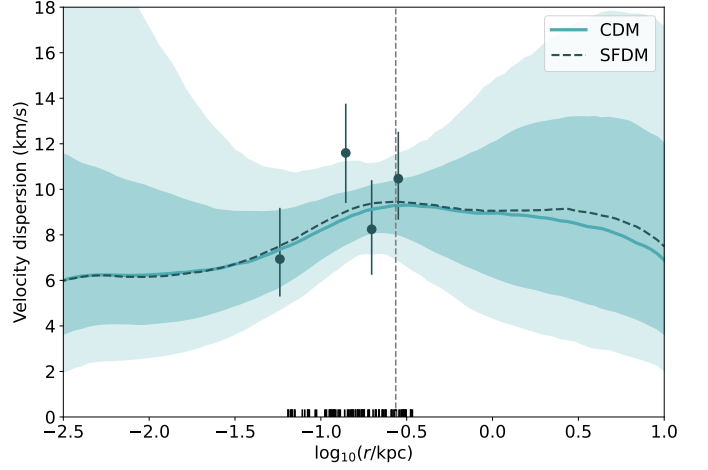


Fig. C.7. Velocity dispersion of Ant B without the 25 stars closest to the centre. The dark blue points represent the binned velocity dispersion previously shown. The best fit from GRAVSPHERE for the CDM model is shown as a solid light blue line, with the light blue shaded regions showing the 68% and 95% confidence intervals for the CDM model. The dashed dark blue line represents the best fit for the SFDM model. Since the best fit for both models is so similar, the confidence intervals for the SFDM model are omitted for clarity. The half-light radius is represented by the vertical dashed line and the bottom marks represent the projected radii of the members of Ant B.

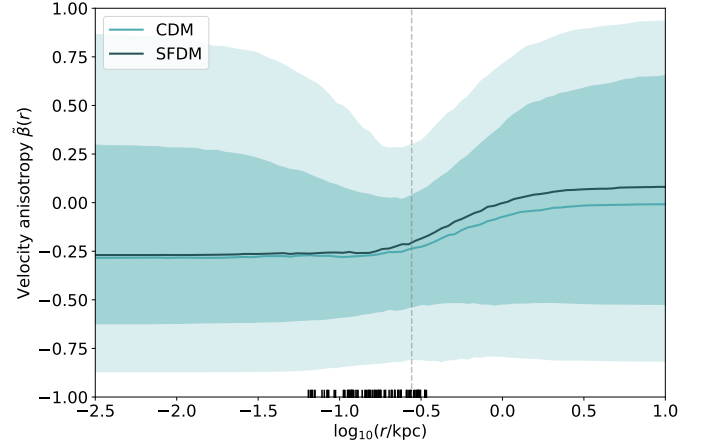


Fig. C.8. Velocity anisotropy profile of Ant B without the 25 stars closest to the centre. The best fit from GRAVSPHERE of the symmetrised anisotropy β for the CDM model is shown as a solid light blue line, with the light blue shaded regions showing the 68% and 95% confidence intervals for the CDM model. The solid dark blue line represents the best fit for the SFDM model. Since the best fit for both models is so similar, the confidence intervals for the SFDM model are omitted for clarity. The half-light radius is represented by the vertical dashed line and the bottom marks represent the projected radii of the members of Ant B.

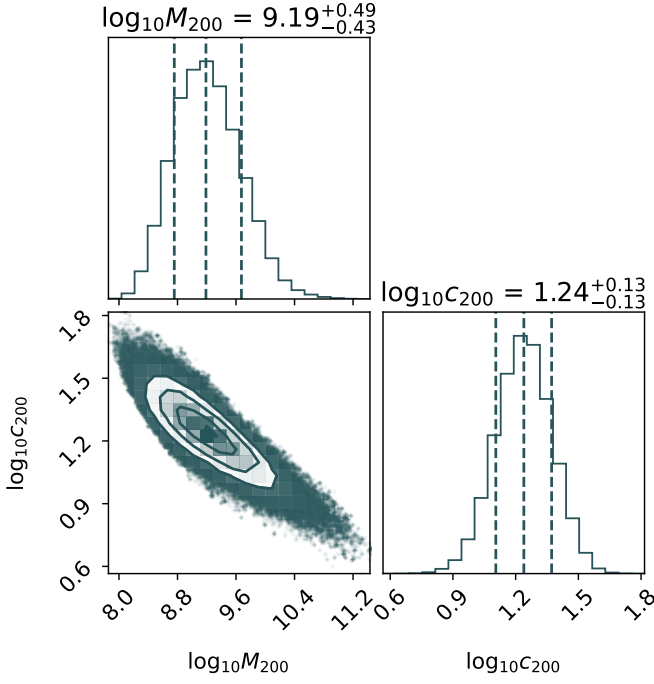


Fig. C.9. Constraints on the CDM profile for Ant B after removing the 25 stars closest to the centre. The histograms along the diagonal represent the posterior distribution for each parameter: the virial mass M_{200} in M_{\odot} and the concentration parameter c_{200} .

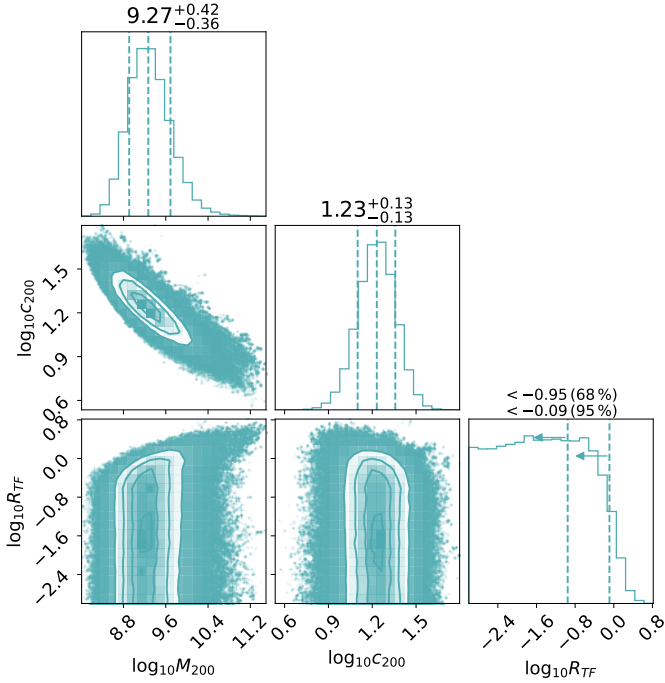


Fig. C.10. Constraints on the SFDM profile for Ant B after removing the 25 stars closest to the centre. The histograms along the diagonal represent the posterior distribution for each parameter: the virial mass M_{200} in M_{\odot} , the concentration parameter c_{200} , and the characteristic length scale of the repulsive self-interaction R_{TF} in kpc.

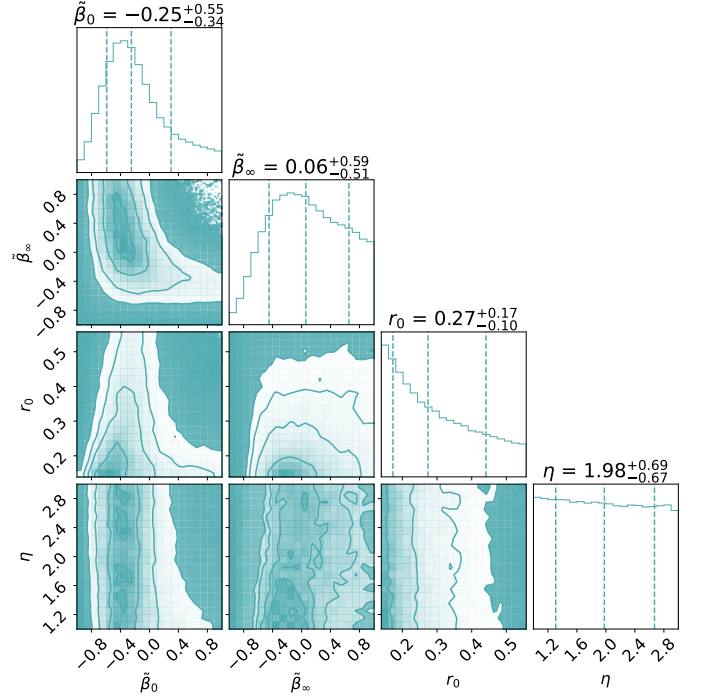
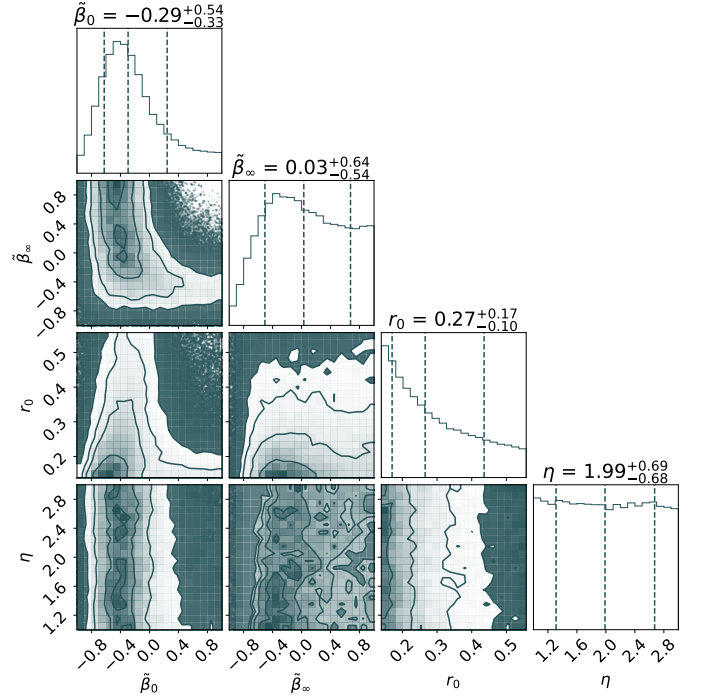


Fig. C.11. Top: Corner plot of the parameters $\tilde{\beta}_0$, $\tilde{\beta}_{\infty}$, r_0 and η of the anisotropy profile for the CDM model without the 25 innermost stars. **Bottom:** Corner plot of the parameters $\tilde{\beta}_0$, $\tilde{\beta}_{\infty}$, r_0 and η of the anisotropy profile for the SFDM model without the 25 innermost stars.